

Modelling the thunderstorm originated downburst event of Vethuizen 2010 for a better insight into storm dynamics



May 2014

Steffan Bos
MSc Meteorology
Wageningen University

Supervisor:

Dr. Leo Kroon (Meteorology & Air Quality, Wageningen UR)

**Modelling the thunderstorm originated downburst event of Vethuizen 2010 for a
better insight into storm dynamics**

S. Bos BSc

Supervisor:
Dr. L. Kroon

May 2014

Wageningen
Meteorology and Air Quality Section
Wageningen University

Photo on cover: Photograph of the leading edge of the squall line of 14 July 2014 near Vethuizen.
(Source: KNMI 2010, photo: Y. van der Heijden)

Abstract

The Western part of Europe is situated in a temperate climate zone. Every year this part of Europe experiences intrusions of warm, moist air from Spain and Central France, which can cause severe storms in Belgium and the Netherlands. Despite an almost yearly occurrence, a lot is unknown of these severe storms.

In this study we take a detailed look, with the Weather Research Forecasting (WRF) model, to the thunderstorm generated downburst event of 14 July 2010, which peaked in intensity in Vethuizen and caused casualties and severe damage throughout the Netherlands. We evaluate the WRF generated output on the thunderstorm squall line event of 14 July 2010 and compare the results of WRF with the RKW-theory, describing the dynamics of squall lines similar as the one occurred on 14 July 2010, as proposed by Rotunno, Klemp and Weisman (1988).

First, the WRF output will be evaluated using a sensitivity analysis of different cumulus and boundary-layer parameterization schemes. For this particular situation, the combination of YSU + WSM6, performs best, in comparison with the cumulus scheme of WSM3 and the boundary-layer schemes MYJ and BouLac, on both the statistical evaluation as the visual evaluation, however the timing was in all runs between 1.5 to 3 hours earlier than the real situation.

Secondly, the RKW-theory will be compared with the WRF output. The RKW-theory states that, in a squall line, the cold pool vorticity (on the cold side) balances the wind shear vorticity (on the warm side) and will therefore result in a perfectly vertical updraft, which is beneficial for storm growth. The theory is overall well represented by the WRF output, especially the vertical updraft, although not all assumptions used for the theory are justified.

Preface

As a child I was fascinated by the thunderstorms that more than yearly occurred over my hometown of Vleuten. I could stand for hours behind my window, just staring at the lightning in the sky. Despite this interest, I started my career of studying at the university in Utrecht, with chemistry. After 2 years I knew I had to know more about weather, and especially (severe) storms, and switched to the Soil, Water, Atmosphere study in Wageningen. After completing my bachelor, I decided to do the master of Meteorology and Air Quality in Wageningen and was I looking forward, mainly to the dynamical courses. I was not let down, and can finally say I've reached the point at which I was able to study the storms I started this study for. After a 6 month period, studying one particular severe event in the Netherlands (Vethuizen, 2010), I learned a lot about the dynamics and the (un)predictability of these storms and can therefore say that I succeeded in my goal I posed before I came to Wageningen.

Table of Contents

1. Introduction	6
2. Background information and theory	7
2.1 Synoptic situation	7
2.2 Downburst dynamics	8
2.3 The Weather Research and Forecasting model	9
2.4 Parameterization schemes	9
2.4.1 Moisture parameterization schemes	9
2.4.2 Boundary-layer parameterization	9
2.5 Cold pool, ambient shear balance and dynamics	10
2.5.1 RKW-theory	10
2.5.2 Horizontal spreading of the cold pool	12
2.5.3 Influence of a rear-inflow jet	13
3. Methodology	15
3.1 Model set-up	15
3.2 Model performance	15
3.2.1 Statistical performance	15
3.2.2 Visual performance	16
3.2.3 Dynamical performance	16
3.2.4 The RKW-theory balance	16
4. Results and discussion	17
4.1 Statistical performance	17
4.2 Visual performance	18
4.3 Dynamical performance	21
4.3.1 Early-mid stage	21
4.3.2 Mid stage	23
4.3.3 End stage	23
4.4 RKW-theory Balance	25
4.4.1 Storm motion	25
4.4.2 RKW-theory tendency	26
4.4.3 RKW-theory assumptions	27
5. Conclusions and future recommendations	30
Acknowledgements	31
Literature references	32
Image references	33
Appendix A, Maximum temperature contour map Europe	34
Appendix B, WRF default settings	35
Appendix C, Model performance checks	36
Appendix D, Overview cross-section locations	37
Appendix E, Early stage: cross-section wind and surface temperature	38
Appendix F, Semi-mid stage: cross-section wind and surface temperature	40
Appendix G, Middle stage: cross-section wind and surface temperature	42

1. Introduction

Most of the western part of Europe (France, Belgium and the Netherlands) is situated in a temperate climate zone with mild winters and moderately warm summers, caused by the influence of the Northern Sea and the northern part of the Atlantic Ocean. This, of course, has implications for the number and severity of thunderstorms. Despite the moderate climate, each year the region experiences some intrusions of warm and humid air masses from southerly currents. Then severe thunderstorms can develop over Western Europe (Hamid 2012). These severe thunderstorms can generate heavy downdraft winds, intense rain and hail, lightning and tornadoes, which can cause serious damage to the (urban) environment (Hamid and Delobbe 2007).

One of these severe thunderstorms was the squall line of Wednesday 14 July 2010. The thunderstorm was initiated over France and then passed over eastern parts of Belgium and the Netherlands. The storm generated a downburst near the village of Vethuizen and caused other wind phenomena throughout the area such as gustnado's and whirlwinds (KNMI 2010 and Groenland et al. 2010), resulting in serious damage throughout the area: trees on railroad tracks, roofs blown away and power masts blown down among other things. Around 6:30 PM local time (16:30 UTC) the storm peaked in intensity (see Fig. 1) and caused in Vethuizen alone a lot of damage. Caravans were blown into a nearby lake, 2 people died and 8 were wounded. The total estimated cost of this storm is around 75 million euros (NOS 2010).

Storms, especially of this intensity, are hard to predict. Not only in occurrence, but mainly their intensity and track. Therefore more research on this subject has to be done.

The objective of this research is to gain a better insight in the processes driving a storm like the one that occurred on 14 July 2010 over Western Europe. This is done by looking at (generalised) theory of downburst events and the dynamics of development of squall lines that can generate downburst winds.

The main objective is to model the Vethuizen 2010 case and to see if the mesoscale weather forecast model (WRF, Skamarock et al. 2008) represents the dynamics and development stages of this storm well, compared with theory and observations. Furthermore, the results of this study will be compared with earlier studies done by the Royal Dutch Meteorological Institute (KNMI, Groenland et al. 2010) and MeteoConsult (Van Dijke et al. 2010). However both papers are mainly damage assessment reports and do not contain a detailed description of the storm dynamics.

To achieve these objectives, the following research questions need to be answered.

Main questions:

- Does the WRF model capture the different development stages of this thunderstorm sufficiently?
- Can the WRF model output be improved by altering the choice of parameterization schemes?

Sub questions:

- What are the different development stages of a (generalised) thunderstorm?
- What are the processes that drive these storms during each development stage?
- How sensitive is WRF model output to changes of parameterization schemes?
- Is WRF able to represent the dynamics of this storm?

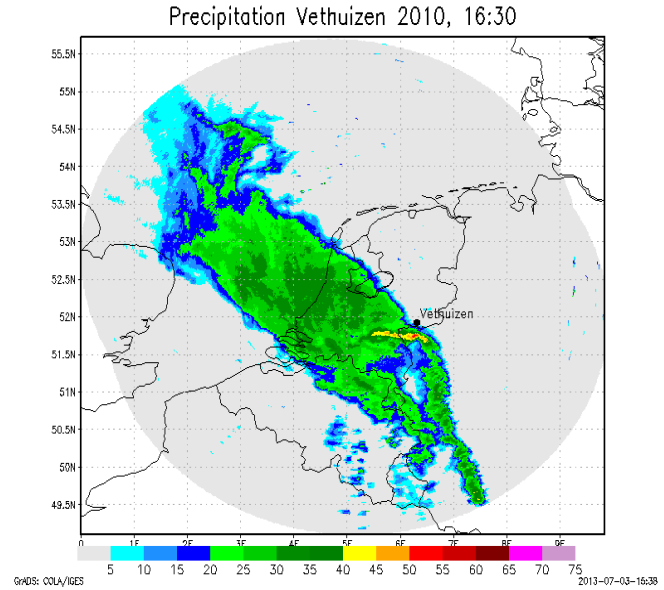


Fig. 1: KNMI radar image for the 14th July 2010, 16:30 UTC, generated by GrADS.

2. Background information and theory

2.1 Synoptic situation

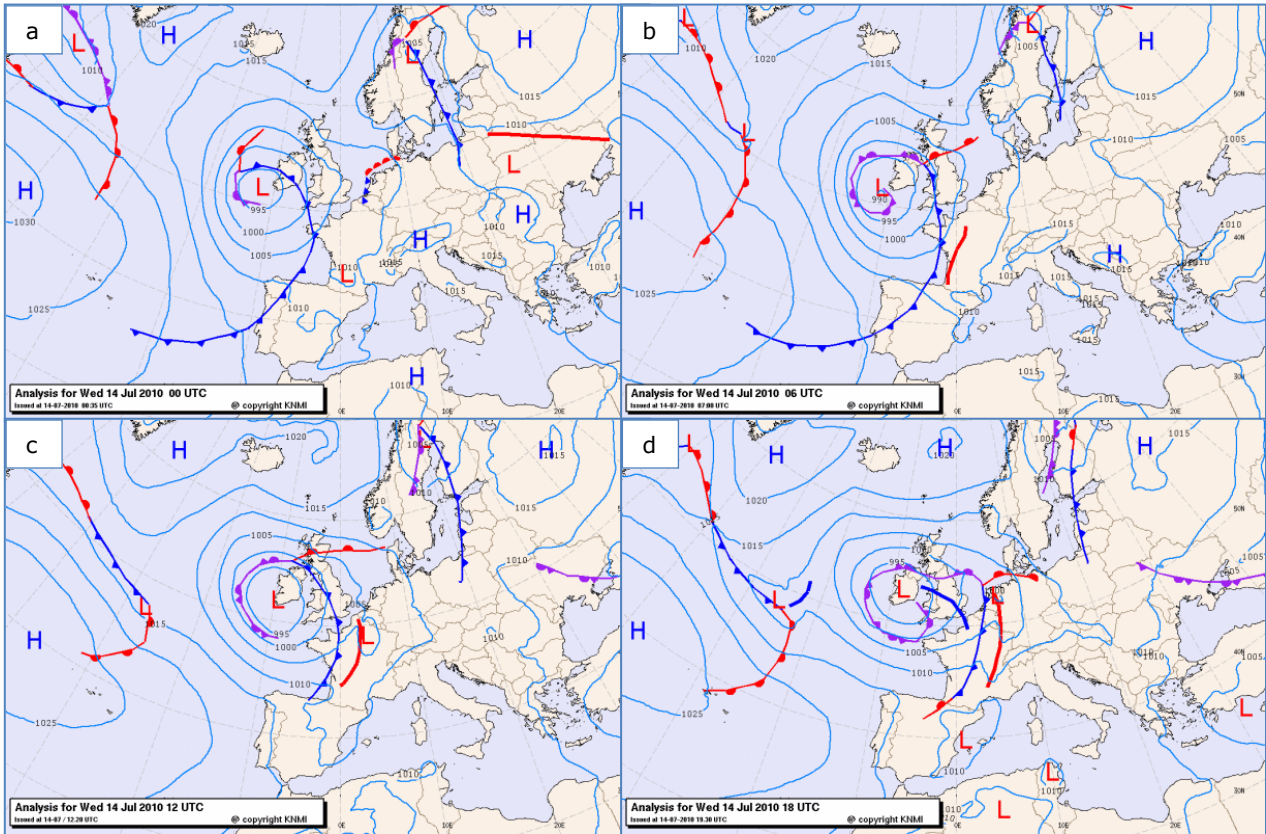


Fig. 2: Synoptic situation of the 14th of July 2010, with a: 00 UTC, b: 6 UTC, c: 12 UTC and d: 18 UTC (KNMI 2013a).

Fig. 2 shows the analysed weather maps of Wednesday 14 July 2010, prior, during and after the storm. The figure shows the presence of a cyclone near Ireland with a central pressure of approximately 990 hPa. Together with the high pressure system over Eastern Europe (approximately 1015 hPa) these systems are responsible for a southerly flow in the Netherlands. In the days prior to and on the 14th of July, an area with high temperatures was present in the greater part of Europe, this can be seen in the temperature map of the 14th of July (Fig. 3, for a view of the temperatures over Europe, see Appendix A). The warmest air, and associated convergence zone, in the region is visible in Fig. 2b,c,d as the red solid line in front of the cold front over Brittany and the Iberian Peninsula. Within the convergence zone over France a thermal low with severe thunderstorms started to develop (Fig. 2c). From this moment on the thunderstorm containing thermal low started to move North-North-Eastwards to the Netherlands. At 18 UTC the thermal low reached the Northern part of the Netherlands (Fig. 2d).

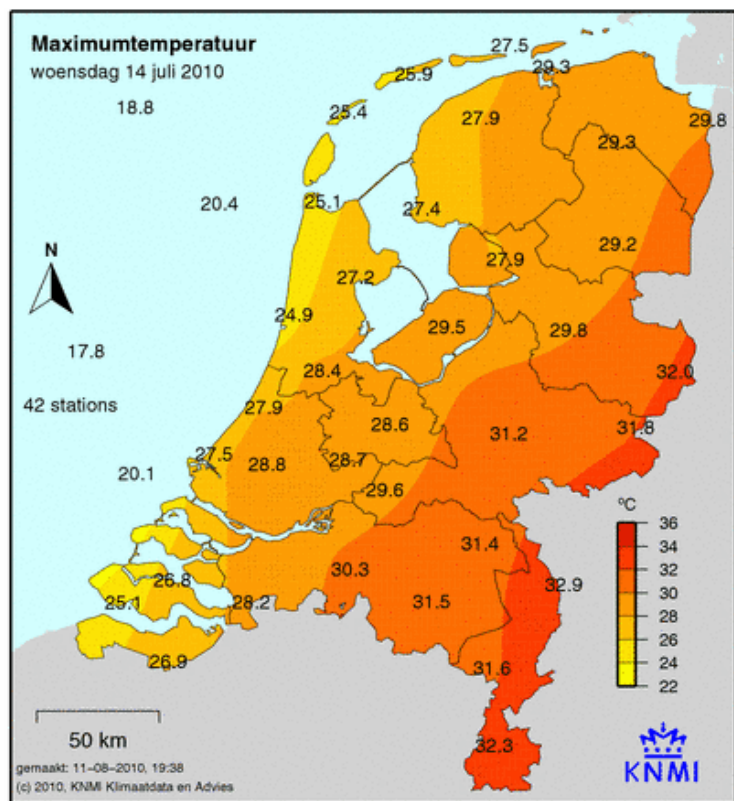


Fig. 3: Maximum temperature of the Netherlands of the 14th of July 2010 (KNMI 2013b)

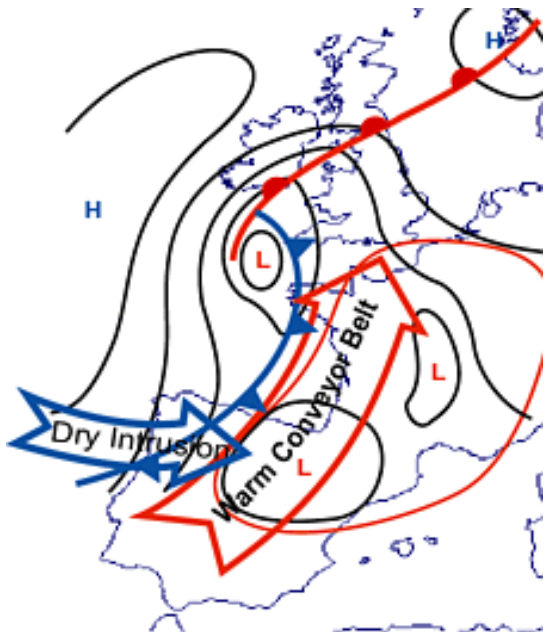


Fig. 4: Low-level flow within Spanish plume. Open red arrow: the warm conveyor belt, open blue arrow: the dry intrusion. Area within red solid line: a typical area of high ThetaE values at 850 hPa. Black solid lines: surface isobars. Classical surface fronts also shown (FMI 2014).

occurs not at the triple point, but in the zone between the warm and cold front. Typically, during a Spanish plume event, the triple point is situated over the British Isles or the North Sea near the Netherlands, indicating a zone of increased convection near or over the Netherlands. This zone of increased convection may influence a storm going over the Netherlands, however the dynamical effect of this zone is not well understood (Weiss and Bluestein 2002) and therefore its influence will not be treated in this paper.

2.2 Downburst dynamics

Downburst events are characterized by strong localized downward flow and a sudden outburst of strong winds near the earth's surface. They typically occur in (severe) thunderstorms or even rain showers, where the weight of the precipitation and the cooling of the air, due to evaporation of (cloud) droplets, acts to accelerate the air downwards. Strong outflow winds develop as the downwards moving air is forced to spread horizontally at the earth's surface (Proctor 1988). Downburst events can also occur in combination with a bow echo, like the one that appeared at Vethuizen, a so called bow-echo-induced downburst event.

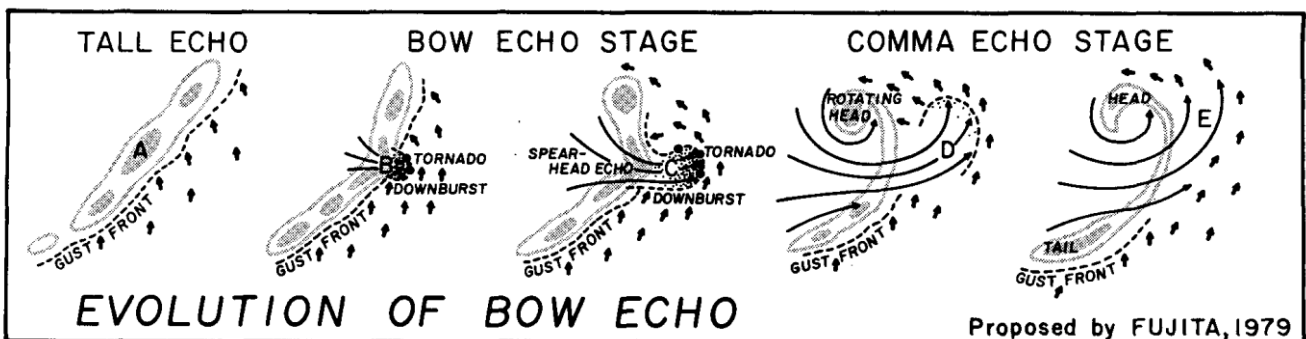


Fig. 5: Evolution of bow echo proposed by Fujita in 1979. In this model, a bow echo is produced by a downburst thunderstorm as the downflow cascades down to the ground. Finally, the horizontal flow of a weakened downburst induced a mesoscale circulation which distorts the initial line echo into a comma-shaped echo with a rotating head (Fujita 1981).

On the basis of both Doppler and radar analysis of several bow-echo-induced downburst events, Fujita (1981) proposed a model of the evolution of a bow echo, see Fig. 5. It starts with a tall thunderstorm with a gust front located along the edge of the activity line (stage A). Next, a downburst descends near the centre of the squall line, distorting the tall thunderstorm echo into a bow-shaped bulge (stage B). The downburst intensifies at the middle of the bow echo. When the downburst reaches its major mature intensity, the bow echo takes the shape of a spearhead (stage C), accompanied by a trench of weak echo

The situation described above shows a similar pattern as a synoptic weather phenomena called 'the Spanish plume'. A Spanish plume event is an event where warm air is lifted from the Iberian Peninsula ahead of an eastward moving upper-level trough over the Bay of Biscay, which is illustrated in Fig. 4 (FMI 2014). If the situation described above further develops and moves towards the northwest, it can cause a trigger effect that causes severe weather in the Benelux region. This trigger effect is reached when the air is, sufficiently moist, potentially unstable and forced to lift. High levels of moisture can be observed over the Mediterranean Sea and the Italian Po Valley. Potential instability is caused by the radiative heating of the surface, creating a thermal low. The forcing mechanism to cause severe thunderstorms is forced lifting by frontogenesis. All these conditions are met at the Iberian Peninsula and when a trough or cut-off low reaches the Peninsula the warm, moist, unstable air will travel North-North-Eastwards to France and can travel even further to the British Isles, the Benelux or Scandinavia (Van Delden 2001).

Typical for a Spanish plume event, is the presence of a triple point. A triple point is a point where 3 different air masses converge. Usually it is the point where the cold-, warm- and occlusion-front intersect. According to Wakimoto (et al. 2006), a zone of increased convection

located along the centre axis of the downburst flow. Downburst-induced tornadoes are likely to form during this stage, since this is the most turbulent phase. As the downburst weakens, a mesoscale circulation dominates the area of the bow echo. Then a rotating head with an appearance of a hook echo forms near the centre of the mesoscale circulation (stage D). In stage E, the final stage, the bow echo often turns into a comma-shaped echo which gradually disappears along with the weakening mesoscale circulation (Fujita 1981, Weisman 2001).

The stage of the storm near Vethuizen was most likely similar to stage C. Being the most turbulent stage, the chance for a downburst is here the highest of all stages.

2.3 The Weather Research and Forecasting model

The Weather Research and Forecast (WRF) model has been developed by a joined effort between the Center for Analysis and Prediction of Storms (CAPS), National Center for Atmospheric Research (NCAR), the Forecast Systems Laboratory and the National Centers for Environmental Prediction of the National Oceanic and Atmospheric Administration (FSL, NCEP/NOAA), with the help of scientists from collaborative universities. The model will provide a framework for both operational numerical weather prediction as well as for research purposes. WRF will target the 1-10km grid scale and is intended for operational weather forecasting, regional climate prediction, air quality simulation and idealized dynamical studies (Michalakes et al 1998). Newer generations of WRF have been developed for a next-generation mesoscale prediction and analysis for understanding mesoscale precipitation systems and to promote closer ties between research and operational forecasting communities (Michalakes 2004).

The framework of WRF uses different parameterization schemes to make the analysis more efficient. It makes use of ECMWF analysed data to feed the boundaries of the system, makes use of the ARW solver to simplify e.g. equations, grid sizes and boundary conditions and makes use of parameterization schemes to solve complicated physical processes. The parameterization schemes include schemes for, microphysics, cumulus physics, surface physics, planetary boundary layer physics and atmospheric radiation physics (Michalakes et al 1998).

For this research project we only alter the choice for the microphysics and planetary boundary schemes, since we believe these two schemes have the greatest influence on the dynamics of the thunderstorm. The next section will describe both parameterization schemes into more detail. The version of WRF used during this research project is WRF version 3.5, which has been released on 18th of April 2013.

2.4 Parameterization schemes

2.4.1 Moisture parameterization schemes

The WRF single-moment microphysics scheme (WSM3) follows Hong et al 2004, including ice sedimentation and other new ice-phase parameterizations. This scheme is especially different from other schemes with its diagnostic relation used for ice-number concentration, which is based on ice mass content rather than temperature. The order of the processes is also optimized to decrease the sensitivity of the scheme to the time step of the model. The WSM3 scheme predicts three categories of hydrometeors: vapour, cloud water/ice, and rain/snow, which is a so-called simple-ice scheme. Like the proposition made by Dudhia in 1989, it assumes cloud water and rain for temperatures above freezing, and cloud ice and snow for temperatures below freezing. This scheme is computationally efficient for the inclusion of ice processes, but lacks super-cooled water and gradual melting rates (Skamarock et al. 2008 and Dudhia 2010).

The WRF single moment six-class scheme (WSM6) extends the WSM3 (and WSM5 which is not described in this paper) scheme to include graupel and its associated processes. The ice-phase behaves differently due to the changes made by Hong et al. in 2004. Dudhia et al. in 2008 proposed a new method for representing the mixed-phase particle fall speeds for snow and graupel particles, by assigning a single fall-speed to both particles that is weighted by their mixing ratios, and applying that fall-speed to both the sedimentation and accretion process (Skamarock et al. 2008 and Dudhia 2010).

The behaviour of the WSM3 and WSM6 schemes differ little for coarse mesoscale grids, but they work much differently on cloud-resolving grids. Of the two WSM schemes, the WSM6 scheme is considered the most suitable for cloud-resolving grids, taking into account the efficiency and theoretical backgrounds (Skamarock et al. 2008 and Dudhia 2010).

2.4.2 Boundary-layer parameterization

The Yonsei University (YSU) planetary boundary layer (PBL) scheme is the next generation of the medium range forecast (MRF) PBL scheme and is widely used. The entrainment is made proportional to the surface buoyancy flux in line with results from studies with large-eddy simulation models like the study of Noh et al. in 2003. The PBL top is defined using a critical bulk Richardson number of zero. The old MRF scheme is effectively dependent on the buoyancy profile, in which the PBL top is defined at the

maximum entrainment layer (compared to the layer at which the diffusivity becomes zero). A smaller magnitude of the counter-gradient mixing in the YSU PBL produces a well-mixed boundary-layer profile (Skamarock et al. 2008, Lemone et al. 2012).

The Mellor-Yamada-Janjić (MYJ) parameterization of turbulence in the PBL and in the free atmosphere, finished by Janjić in 2002, represents a non-singular (the associated matrix has an inverse) implementation of the Mellor-Yamada Level 2.5 turbulence closure model, proposed by Mellor and Yamada in 1982, for the full range of atmospheric turbulent regimes. The upper limit of the MYJ scheme depends both on the TKE as well as the buoyancy and shear of the driving forces. In the unstable range, the functional form of the upper limit is derived from the requirement that the TKE production is non-singular in the case of growing turbulence. However, in the stable range, the upper limit is derived from the requirement that the ratio of the variance of vertical velocity deviation and TKE cannot be smaller than the regime of vanishing turbulence. The TKE production/dissipation differential equation is solved iteratively (Skamarock et al. 2008). MYJ is, similar to YSU, widely used in the meteorological community (Lemone et al. 2012).

The Bougeault and LaCarrere (BouLac) parameterization scheme is comparable with the MYJ scheme, mainly because both schemes depend on the TKE production/dissipation. However, where the MYJ scheme uses a 2.5 level turbulence closure model, BouLac uses a 1.5 level turbulence closure model. The length scale of the model predicted by the BouLac scheme is determined by its initial velocity, depending on the TKE at this particular height, where the length scale for MYJ is found iteratively (Lemone et al. 2012). This parameterization scheme is used by Putsay (et al. 2011) for their analysis of the Pukkelpop storm of 2011 and will therefore also be tried here.

According to current research, MYJ has a colder bias than the YSU scheme (Pagowski 2004 and Hu et al. 2010), which leads to a prediction of shallower boundary layers. Despite this prediction, MYJ also predicts more moisture in the BL and a stronger capping inversion than the YSU (Weisman et al. 2008). However, Wisse and Vilà (2004) stated that the MRF scheme (predecessor of YSU) predicts more widespread precipitation with a higher average accumulated precipitation and is better suited for active convective weather than other PBL schemes. All this has an effect on how the model will predict convective storms.

2.5 Cold pool, ambient shear balance and dynamics

2.5.1 RKW-theory

The RKW theory is named after its proponents, Rotunno, Klemp and Weisman (Rotunno et al. 1988), who introduced the theory for squall lines in 1988. The theory is based on a large number of 3D-simulations conducted in the mid-1980's. Their conclusion was that a broad range of convective structures could be produced by numerical models by changing only the environmental shear profile (Bryan 2012). The RKW theory starts with the Boussinesq equation, of a frictionless moving air parcel, governing the component of the vorticity directed along a hypothetical line-invariant disturbance.

$$\rho_0 \frac{d}{dt} \frac{\eta}{\rho_0} = - \frac{\partial B}{\partial x} \quad (1)$$

Where

$$\eta \equiv \frac{\partial u}{\partial z} - \frac{\partial w}{\partial x} \quad (2)$$

And

$$B = g \frac{\Delta \theta}{\theta_0} \quad (3)$$

η is the vorticity in the along line (y)-direction; $\rho_0(z)$, the base-state density; B , the total buoyancy; u , the cross-line velocity; w , the vertical velocity; g , the gravitational constant; $\Delta \theta$, potential temperature deficit between the cold pool and its surrounding; θ_0 , the average surface temperature; x , the cross-line distance; z , the altitude; t , the time and d/dt , the rate of change with time following a parcel.

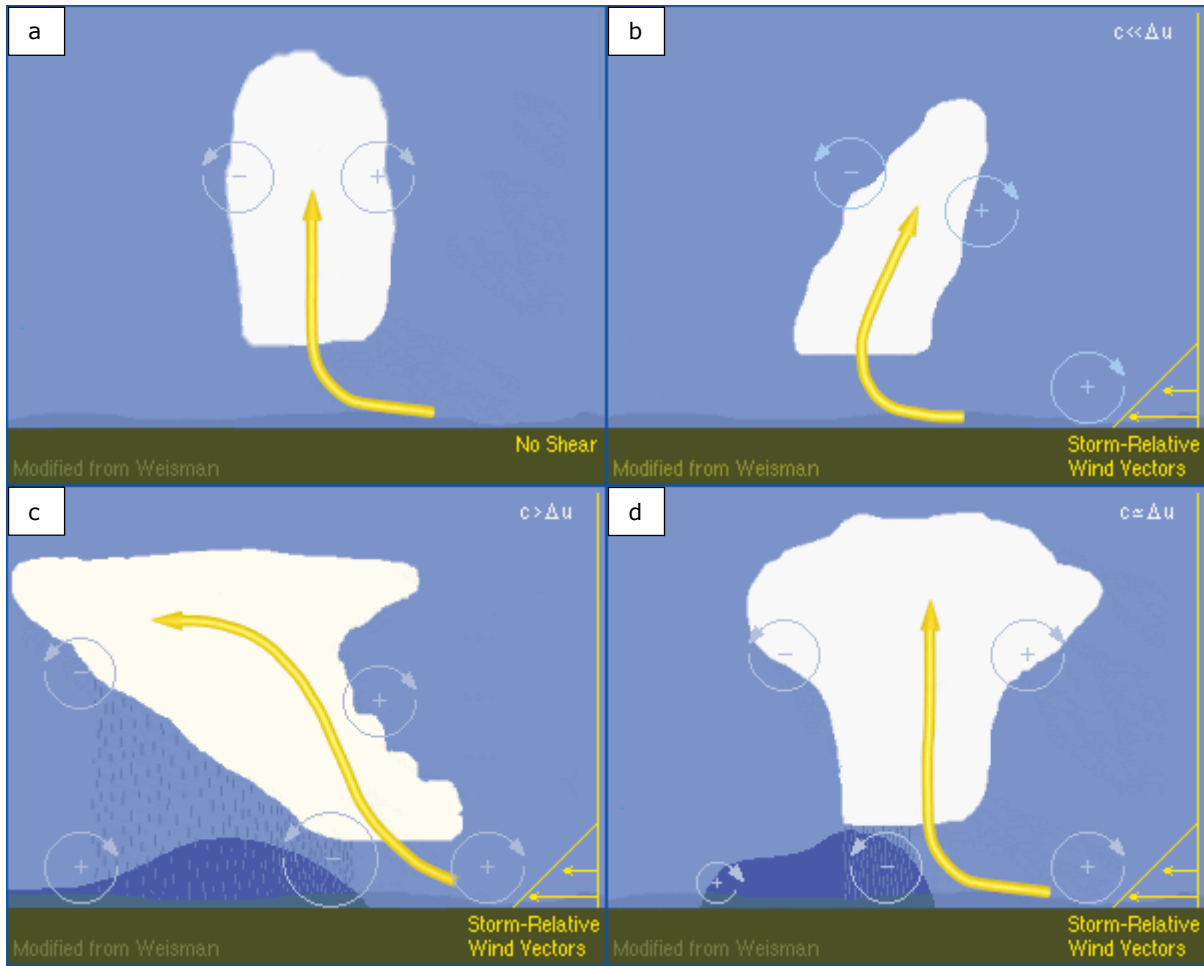


Fig. 6: Schematic diagram showing how a buoyant updraft may be influenced by wind shear and/or a cold pool. (a) With no shear and no cold pool, the axis of the updraft produced by the thermally created, symmetric vorticity distribution is vertical. (b) With shear, the distribution is biased toward positive vorticity and this causes the updraft to lean back over the cold pool. (c) With a relatively strong cold pool, the distribution is biased by the negative vorticity of the underlying cold pool and causes the updraft to lean upshear. (d) With both a cold pool and shear, the two effects may negate each other, and allow an erect updraft (Weisman et al. 1999).

If we look at a situation of a particle with only buoyancy, illustrated in Fig. 6a with the arrow indicating the maximum buoyancy, we see that the right hand side of equation 1 creates positive vorticity (decreasing buoyancy with increasing x , $-\frac{\partial B}{\partial x} > 0$) on the right side of the maximum buoyancy and negative vorticity (decreasing buoyancy with decreasing x , $-\frac{\partial B}{\partial x} < 0$) on the left side of the maximum buoyancy which, in equal amounts, is resulting in a perfectly vertical upward flow. Next we consider the same situation, only the particle on the right side starts with vorticity generated by wind shear, as illustrated in Fig. 6b. The vorticity generated by wind shear is positive, according to equation 2, since $\partial u / \partial z$ is positive. Because the particle starts with an extra positive vorticity, the flow will not be perfectly vertical, but skewed in the downshear direction.

In situations with upward flow, as described above, we usually find precipitation. Precipitation forms a cold pool, by the evaporation, sublimation and/or melting of precipitation, precipitation drag and vertical perturbations in the pressure gradient (Corfidi 2003). Due to the negative buoyancy (downward motion), generated by precipitation, in the middle of the cold pool, we get the exact opposite situation in the cold pool of the only upward motion generated by positive buoyancy seen in Fig. 6a. Buoyancy increases with increasing x in the left side of the cold pool generating a negative vorticity. At the right side of the cold pool it is the other way around, generating a positive vorticity (Fig. 6c). The presence of cold pool generated vorticity lets the air parcel flow over the cold pool, resulting in a skewed vertical updraft in the upshear direction. If we also include the wind shear in the situation, the vorticity associated with this wind shear can change the direction in the upward flow and “*if the circulation with the cold pool’s negative vorticity approximately balances the circulation associated with the positive vorticity of the low-level shear*”, the flow turns perfectly vertical again (Fig. 6d, Rotunno et al. 1988).

To reach a quantitative criterion for the low-level shear to balance a cold pool, the RKW-theory writes equation 1 without further approximation, as

$$\frac{\partial \eta}{\partial t} = -\frac{\partial}{\partial x}(u\eta) - \frac{\partial}{\partial z}(w\eta) - \frac{\partial B}{\partial x} \quad (4)$$

Fixing the frame of reference moving with the leading edge of the cold pool and integrating equation 4 from the left boundary (L), giving $x = L$, to the right boundary (R), giving $x = R$, of the edge of the cold pool, and from the ground to a restricted height (d), giving $z = d$ (Fig. 7), they obtained

$$\frac{\partial}{\partial t} \int_L^R \int_0^d \eta dz dx = \int_0^d (u\eta)_L dz - \int_0^d (u\eta)_R dz - \int_L^R (w\eta)_d dx + \int_0^d (B_L - B_R) dz$$

Tendency flux at left flux at right flux at top net generation

(5)

Equation 5 is the most important equation, called ‘the balance equation’, and this paper will evaluate this equation on the WRF output. They further assumed that there is a steady state, setting the tendency to zero and assumed that there is negligible buoyancy of the air approaching the cold pool, $B_R = 0$. They also took the vorticity (η) left from the cold pool edge. Under these assumptions, equation 5 reduces to

$$0 = \left(\frac{u_{L,d}^2}{2} - \frac{u_{L,0}^2}{2} \right) - \left(\frac{u_{R,d}^2}{2} - \frac{u_{R,0}^2}{2} \right) - \int_L^R (w\eta)_d dx + \int_0^d B_L dz \quad (6)$$

For the next step they assumed that the cold air is stagnant (relative to the cold pool edge), so that $U_{L,0} = 0$, and the buoyancy is only limited to the height of the cold pool (H), giving $z = H$, where $H < d$. With these simplifications, equation 6 becomes

$$0 = \frac{u_{L,d}^2}{2} - \left(\frac{u_{R,d}^2}{2} - \frac{u_{R,0}^2}{2} \right) - \int_L^R (w\eta)_d dx + \int_0^H B_L dz \quad (7)$$

Considering the first case, with no shear at the right boundary and a rigid plate at the restricted height, the second and third term vanish, resulting in

$$u_{L,d}^2 = 2 \int_0^H (-B_L) dz \equiv c^2 \quad (8)$$

And if taking the last case in mind, including shear and a cold pool, looking for the optimal state where the low-level flow is turned by the cold pool in such a way that there is a perfectly vertical updraft, $U_{L,d}$, $U_{R,d}$ and $\int_L^R (w\eta)_d dx$ are set to 0, to obtain

$$\Delta u = c \quad (9)$$

where

$$\Delta u \equiv u_{R,d} - u_{R,0} = -u_{R,0} \quad (10)$$

In this research project, we test the balance equation as well as the assumptions made after the balance equation with the WRF generated output in order to research the significance of each term in the balance equation and the correctness of the assumptions that were made.

2.5.2 Horizontal spreading of the cold pool

As described in section 2.5.1, the RKW-theory states that the ratio $c/\Delta u = 1$ is ideal for the formation of strong thunderstorms, but it also describes different situations where there is an imbalance between the two (Fig. 6). This section will explain more about the horizontal extent associated with the description of the RKW-theory.

The RKW-theory roughly states there are 3 different stages of storm development, the early stage, the mid stage and the end stage. The RKW-theory states that due to the updraft of water particles, rain will occur if the droplets are large enough. The precipitation area in the very start of a raining event is very narrow and its vertical picture will look somewhat similar as the situation shown in Fig. 6a, only now we also have a small precipitation area. This precipitation will start the formation of the cold pool. When the sequence of new convective cells strengthen the cold pool, the balance of $c/\Delta u = 1$ will take place. This may only happen when the ambient shear circulation is not extremely strong. Due to this balance, air at the leading edge of the cold pool will be lifted vertically, which results in a deeper and stronger lifting

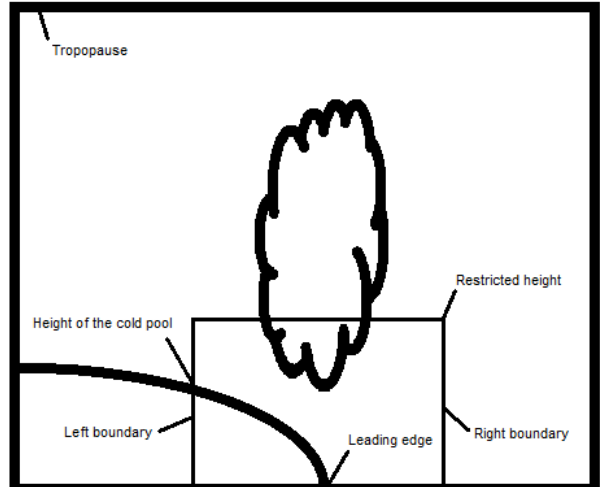


Fig. 7: Schematic diagram illustrating the position of different boundaries used to quantify the RKW-theory.

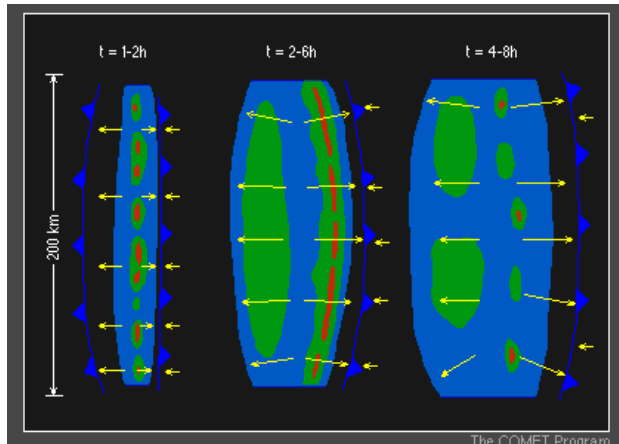


Fig. 8: Horizontal overview of the precipitation and cold pool development for the different stages (Weisman et al. 1999).

and tilts more. This will continue until the tilt is so large that the storm will cut itself off from its own energy source (warm, moist air). This phase initiates the dissipation phase of the storm (Fig. 8 t=4-8h).

2.5.3 Influence of a rear-inflow jet

In the case of a relatively strong rear inflow jet, which was present during the storm of Vethuizen (Groenland et al. 2010), the balance of $c/\Delta u = 1$ remains longer present in the lower part of the storm, resulting in a more vertically erect structure (Fig. 10b). This situation is typical for environments with high CAPE values and relatively strong shear, and is associated with the development of severe long-lived bow echoes and, when this stage remains present for several hours, allowing the cold pool to become extremely strong before the system begins to tilt upshear. When the system does tilt upshear, it produces an extremely warm front-to-rear ascending current, which continues to warm up the air above the cold pool. This enhances the strength of the rear inflow jet (Rotunno et al. 1988 and Weisman and Rotunno 2004).

(Fig. 6d). Usually, the strongest storms are observed during this phase of the storm development. Because the convective cells move with approximately the same speed as the cold pool, the line of convection remains relatively narrow. Fig. 8 t=1-2h gives a horizontal example of the cold pool in this particular stage of the cold pool formation.

As the cold pool stretches backward (Fig. 8 t=2-6h) and continues to strengthen. After 4 hours after the cold pool developed, the cold pool circulation starts to dominate the ambient wind shear circulation ($c > \Delta u$) and the cells tilt upshear (Fig. 6c). The line of convection starts to become less. Due to the tilt upshear, an area with lighter precipitation will form behind the leading line of convection. As the cold pool strengthens more, the spread will become larger

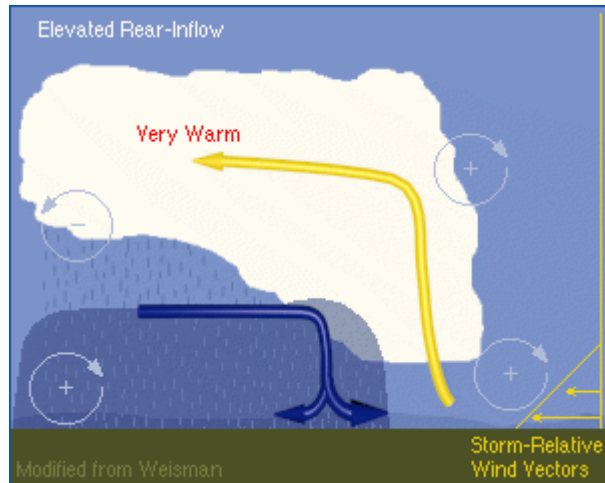


Fig. 9: Strong cold pool circulation with a rear-inflow jet which leads to surface winds (Weisman et al 1999).

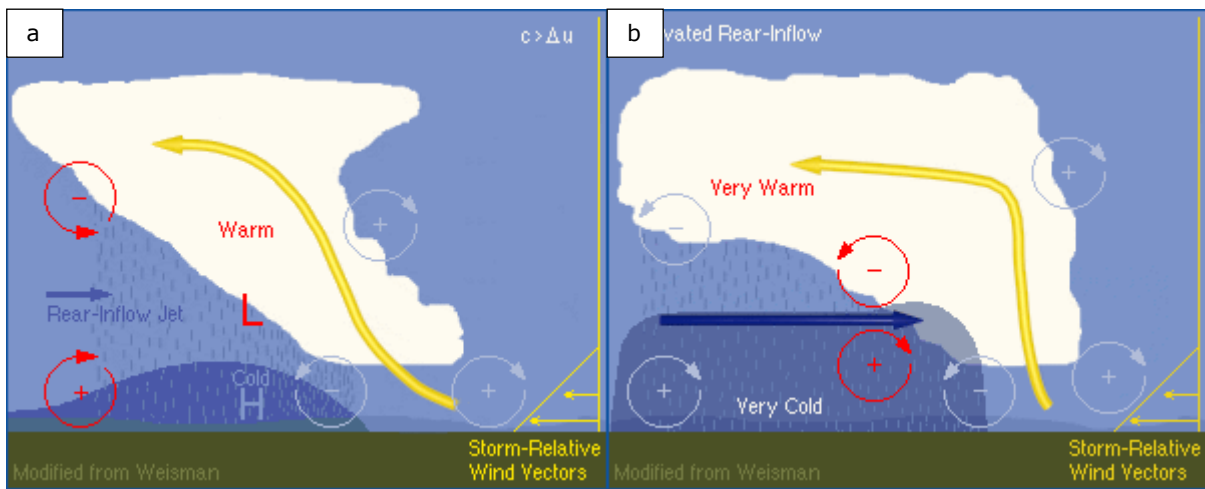


Fig. 10: Generalised development stages of thunderstorms. (a) Cold pool circulation dominates shear circulation, despite the presence of a weak rear-inflow jet. (b) Strong cold pool circulation with a developed rear-inflow jet (Weisman et al. 1999).

The damaging winds associated with (severe) bow-echoes are the result of both the downward transport of momentum from the descending rear-inflow jet, which spreads along the surface, as well as the extremely strong cold pool (which accelerates the air outward due to the large hydrostatic pressure difference, Fig.9, Weisman et al. 1999).

3. Methodology

3.1 Model set-up

The analysis exists of four parts, containing statistical performance, visual performance, dynamical performance and the RKW-theory balance, all based on the WRF generated output of 14 July 2010. WRF version 3.5 was used to conduct a 66-hour simulation over the research area, containing a great part of France and Belgium, Luxembourg and the Netherlands, the exact domain can be seen in Fig 11. The simulation started on 13 July 2010 at 00 UTC to include the 24 hours of spin-up time needed for the model to run a stable simulation. Because of the nature of spin-up time, it will be not included in the analysis. To feed the boundaries for the system, $0.125^\circ \times 0.125^\circ$ ECMWF analysed files are used.

To answer the second main research question, parameterization schemes for the WRF model runs will be changed in order to investigate their contribution to the model output. Two types of parameterization schemes are changed, the moisture scheme (WSM3 and WSM6) and the boundary layer scheme (MYJ, YSU and BouLac). However there is a third type of parameterization scheme that will be changed, surface physics (sf-clay) parameterization scheme, but that will not be explained in this paper since it is coupled to the boundary layer scheme. Information about the specific runs is visible in Table 1.

The model output will be evaluated with different model performance checks to see which parameterization combination predicts the storm with the highest accuracy. The different model performance checks will be described in the next section.

Table 1: Parameterization for moisture, boundary and coupled surface schemes for the different runs. A complete overview of all the parameterizations schemes used for the runs can be seen in Appendix B, WRF default settings.

Run	Moisture scheme	Boundary layer scheme	Sf-clay scheme
WSM6 + MYJ	WSM6	Mellor-Yamada-Janjić	Monin-Obukhov Janjić
WSM3 + MYJ	WSM3	Mellor-Yamada-Janjić	Monin-Obukhov Janjić
WSM6 + YSU	WSM6	Yonsei University	Monin-Obukhov
WSM3 + YSU	WSM3	Yonsei University	Monin-Obukhov
WSM6 + BouLac	WSM6	Bougeault and Lacarrere	Monin-Obukhov Janjić
WSM3 + BouLac	WSM3	Bougeault and Lacarrere	Monin-Obukhov Janjić

3.2 Model performance

The performance of each model output will be evaluated in four different ways. Section 3.2.1 will explain more about the statistical performance, section 3.2.2 will contain the visual performance, section 3.2.3 will describe the dynamical performance and most important, section 3.2.4 will explain the influence of the RKW theory, and its assumptions, to the model output.

3.2.1 Statistical performance

The statistical performance will contain a comparison of the timing and temperature tendency modelled for Vethuizen and a statistical parameter check for four different stations. The model output for temperature and pressure (two of the four stations) will be compared with the observed KNMI data for the stations: Arcen, Deelen, Hupsel and Volkel. These stations are chosen based on their position near Vethuizen. The exact position of these stations can be seen in Fig. 12. The statistical parameters used are:

1. The mean bias error (MBE) is average of the difference between the model predicted variable at point i (P_i) and the observed variable at point i (O_i).

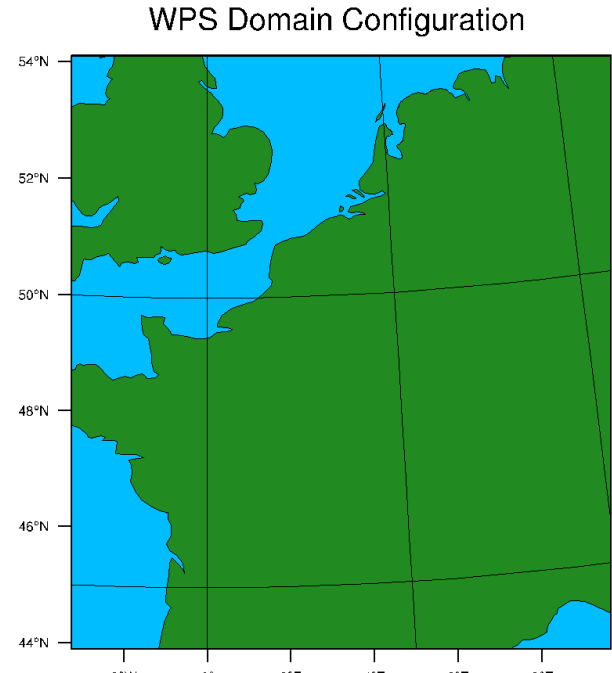


Fig. 11: WRF domain used for conducting all the runs

$$MBE = N^{-1} \sum_{i=1}^N (P_i - O_i) \quad (11)$$

2. The median of the bias error (Med-BE) is the median of the bias difference.

$$Med-BE = \text{Median} (P_i - O_i) \quad (12)$$

3. The root mean square error (RMSE) is the root of the mean square error (MSE), which is the average of the squared error between model predicted value at point i and the observed value at point i .

$$RMSE = \left(N^{-1} \sum_{i=1}^N (P_i - O_i)^2 \right)^{\frac{1}{2}} \quad (13)$$

4. The mean absolute error (MAE) is the average of the absolute difference between the model predicted value at point i and the observed value at point i .

$$MAE = N^{-1} \sum_{i=1}^N |P_i - O_i| \quad (14)$$

5. The median of the absolute error (Med-AE) is the median of the absolute difference.

$$Med-AE = \text{Median} |P_i - O_i| \quad (15)$$

The parameter Med-AE is taken as the most solid parameter and best indicator of the model performance, since it is not very vulnerable for outliers and contains the absolute error, a bias error can be averaged out. Apart from these statistical parameters, scientific evaluation can be enhanced by examination of graphical data display (Willmott, 1982), as will be discussed in the next sections.



Fig. 12: Location of the statistical performance stations (Google Earth 2013).

3.2.2 Visual performance

For the visual performance, the WRF cloud output will be compared with the observed satellite cloud data. The goal here is to see whether or not the model predicted clouds at the right location and right time, the right order of magnitude as well as the right cloud patterns. Besides clouds themselves, we also glance at the cloud top temperatures and corresponding ice formation in the WRF output in order to look at the approximate height of the system.

3.2.3 Dynamical performance

For the dynamical performance, we will take a look at the explained dynamics, focussing on the visual aspect of the cold pool strength c and wind shear Δu (section 2.5), and how the model represents these dynamics. The quality will be determined by a comparison with the theory, no quantified representation of data will be shown in this section. The goal is to find areas where there is an perfectly vertical upward motion (c balances out Δu and), as the theory suggests, these areas are at the leading edge of the squall line.

3.2.4 The RKW-theory balance

The RKW-theory balance describes how well the balance equation (equation 5), as well as the assumptions following the balance equation, are described by the WRF-model output. We take a box with certain height and width and make a balance of the vorticity of this system. The frame of reference for the box is the leading edge of the cold pool, meaning that the storm relative motion will be deducted from the wind speed from the WRF output. However, this will not influence the vorticity itself, but will influence the balance of the balance equation.

4. Results and discussion

4.1 Statistical performance

The statistical performance is checked on four stations, Arcen, Deelen, Hupsel and Volkel. All stations have observed hourly data, for temperature. Only two stations, Deelen and Volkel, contain also pressure data. Therefore there are in total 20 checks for temperature and 10 for pressure. The checks will exclude the 24 hours spin-up time. For each run at each station, the check will be performed and if this check is the best for each run, it gets the score +1. If the Med-AE belongs to this run, the number will also be presented between the brackets. Table 2 contains the result.

Table 2: Model performance check for the stations Deelen (T and P), Volkel (T and P), Arcen (T) and Hupsel (T). If the model performs best for a certain check (5 per station, 20 in total for T, 10 in total for P), it gets the score +1. The number between the brackets is the times Med-AE belongs to this run for the atmospheric property.

	Temperature	Pressure	Total
MYJ + WSM6	0	0	0
MYJ + WSM3	0	10(2)	10(2)
YSU + WSM6	8(2)	0	8(2)
YSU + WSM3	6(2)	0	6(2)
BouLac + WSM6	3(0)	0	3(0)
BouLac + WSM3	3(0)	0	3(0)

What is clearly visible is that MYJ + WSM3 is the best setting to predict the best pressure over this domain. All 10 checks were in favour of this particular run. For the temperature the best performing checks are more scattered, although none of the checks were in favour of the MYJ boundary-layer scheme. Looking at Table 2, it is visible that the runs with YSU perform better than the runs with MYJ or BouLac. There is a small difference between the different moisture schemes, to see the exact results for the parameter checks, see Appendix C, Model performance checks. To see which of the two performs best, we also look at the timing of the front passage.

Fig. 13 shows the hourly observations and hourly model output for Arcen, for each run. The observations show a cold front passage between 16:00 and 17:00 UTC, with a temperature drop of 11.1 °C. All the model runs show a similar pattern, starting with lower temperatures at night, showing a similar pattern as the observations once the temperature increases during the morning. This pattern stays the same till 11:00 UTC. After 11:00 UTC all runs show a temperature drop, which is caused by a passage of a small rain area. After this drop, all models, except MYJ + WSM3, show a rise in temperature again. Then between 13:00 and 14:00 the cold pool passes over Arcen for MYJ + WSM6, MYJ + WSM3 and YSU + WSM3, and passes between 14:00 and 15:00 for YSU + WSM6 and BouLac + WSM6, which is significantly earlier than the observed cold pool passage. Also, all model runs have a significantly lower maximum temperature. YSU + WSM6 has the highest maximum temperature of all the model runs, with 29,8 °C (observed maximum temperature is 32,0 °C). Because all models have their timing wrong, the MBE is negative for all runs (showing there is a cold bias over the entire simulation). Fig. 13 also shows that the MYJ runs have an overall colder profile than the YSU runs, confirming the results of the research of Pagowski 2004 and Hu et al. 2010.

According to the results presented by Table 2 and Fig. 13, the run YSU + WSM6 performs better than the other parameterization scheme combinations on a great part of the model performance checks and timing. Therefore for not overwhelm this paper with pictures, only the pictures of the results of run YSU + WSM6 will be shown in the main paper. For the analysis however, all results will be taken into account and are visible in Appendices E, F and G.

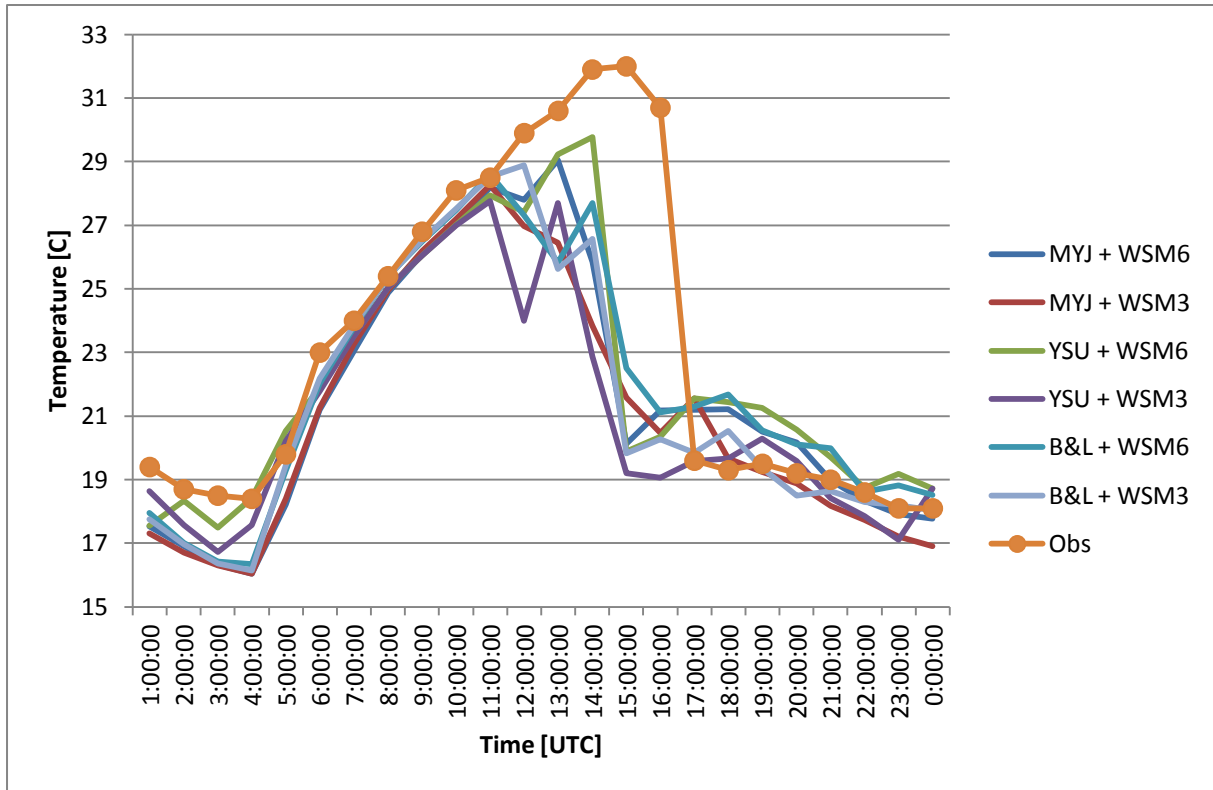


Fig. 13: Comparison between hourly modelled and hourly observed temperature [C], for Arcen 14, 1:00 till 15, 0:00 UTC, July 2010.

4.2 Visual performance

As section 3.2.2 described, We compare the satellite images, with WRF generated output. This will be focussed at the starting stage and the middle stage. This is done, because only the 3 hour Meteosat MSG-2 satellite images are free to use, the Meteosat MSG-2 takes pictures every 15 minutes (ESA 2012).

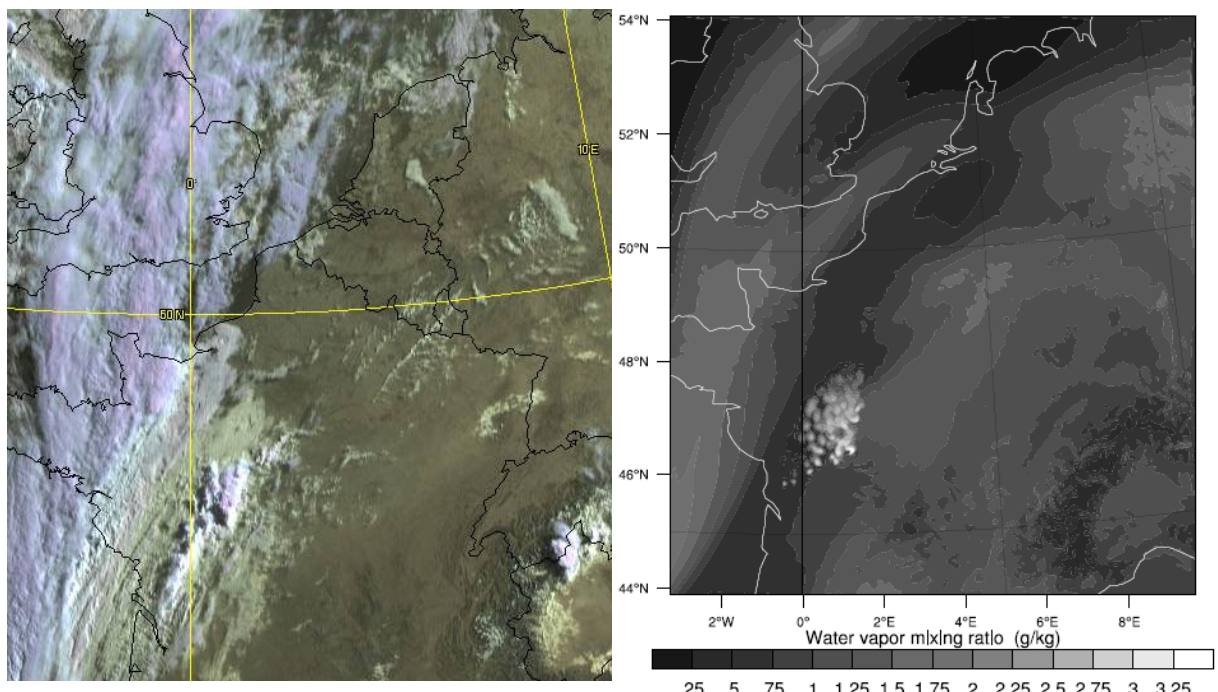


Fig.14: Meteosat MSG-2 satellite image (left, EUMETSAT 2010a) compared with the water vapour mixing ratio (right) at eta level 17 (approx. 7500m) for 14 July 2010, 6:00 UTC.

Fig. 14 compares the Meteosat MSG-2 satellite image with the WRF generated water vapour mixing ratio at approximately 7500m (eta level 17). The satellite image clearly shows an area over West-France, starting North from Bordeaux, with relatively high clouds. This same area is also highlighted by the WRF image, with increased water vapour mixing at 7500m. Also, the satellite image shows the cold frontal cloud band, which is laying over Bretagne and the United Kingdom. Looking at the WRF image, the same cold frontal band is present over the same area as the satellite image. Also the small pocket of clouds over the North Sea, West of the Netherlands and Belgium is present in both images, although the WRF image shows a connecting with the cold frontal band, while the satellite picture has the same pocket disconnected from the cold frontal band.

To gain a better insight in the model development, we also looked at the satellite image and WRF generated image 6 hours later. This is shown in Fig. 15. Unlike Fig. 14, this figure shows a clear difference between the two images. The satellite image shows one thick band with dense clouds over the Southern part of the Netherlands, Belgium and the North-Eastern part of France. The WRF image shows 2 bands with increased water vapour, indicating the presence of two bands of dense clouds. One band over Belgium and North-Eastern France and a second band over the Netherlands and Western part of Germany. The second band over the Netherlands is generated by the thermal low, which originated over France around 6 UTC. This band of clouds is, in the satellite image, incorporated in the dense band generated by the cold front.

The second band associated with the presence of a thermal low is the main reason for the presence of the second band and mainly its timing. As shown in Fig. 13, the timing of the passage of this thermal low is approximately 2 hours earlier than the observed passage. This pattern of two precipitation bands was visible for all model runs and may lead to less intensive precipitation modelled by WRF. However, since the thermal low precipitation is decoupled from the cold frontal precipitation, the effects proposed by the RKW-theory are more visible in the WRF generated output, than in the real case, since the RKW-theory in the real case may be disturbed and/or enhanced by the coupling with the cold front.

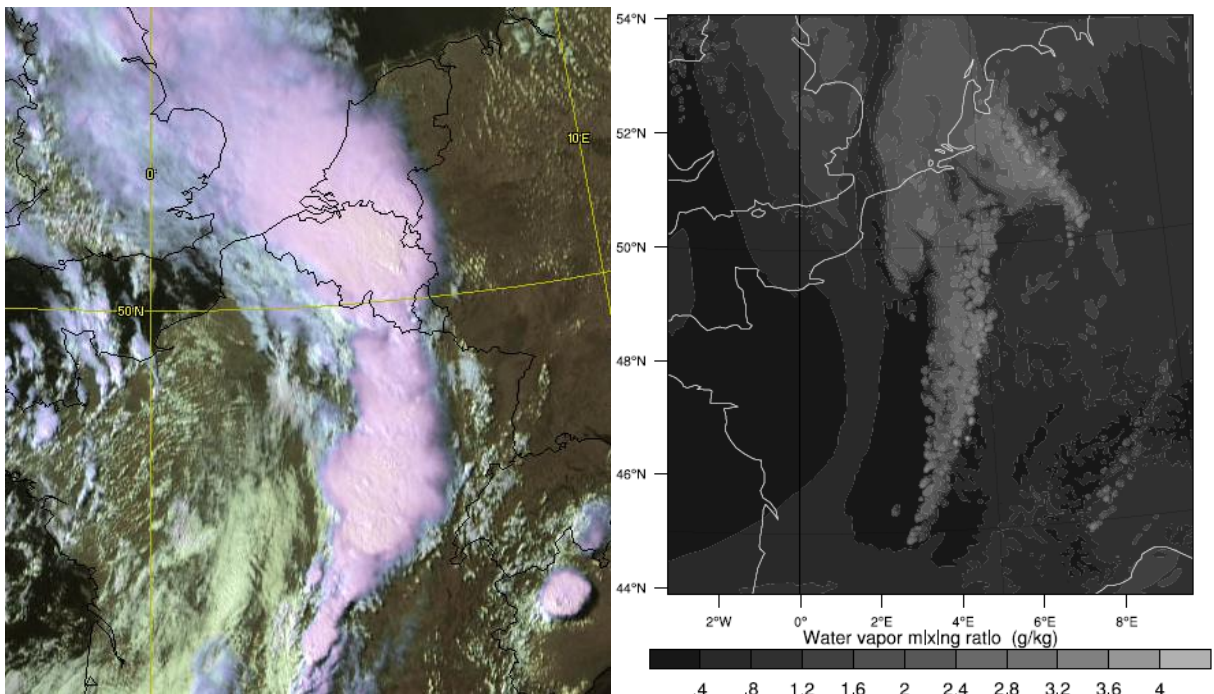


Fig. 15: Meteosat MSG-2 satellite image (left, EUMETSAT 2010a) compared with the water vapour mixing ratio (right) at eta level 17 (approx. 7500m) for 14 July 2010, 15:00 UTC.

We also compared the Meteosat HRPT cloud top satellite image with the WRF generated ice mixing ratio at approximately 13km. The comparison can be seen in Fig. 16. The satellite image shows very cold cloud tops ($>-50^{\circ}\text{C}$) over Northern-France, indicating relatively high clouds. At the same regions, in order to generate high clouds, the WRF model should have modelled increased values of ice mixing ratio and these regions are visible in the WRF generated image. The area with relatively high ice mixing ratio values has been shifted marginally to the left. The cold front, as discussed above, has not developed ice particles above 13km in the WRF generated output. However, in the satellite image we see a small band with cloud top temperatures, below -40°C , over the English Channel associated with the cold front, which indicates convective weather.

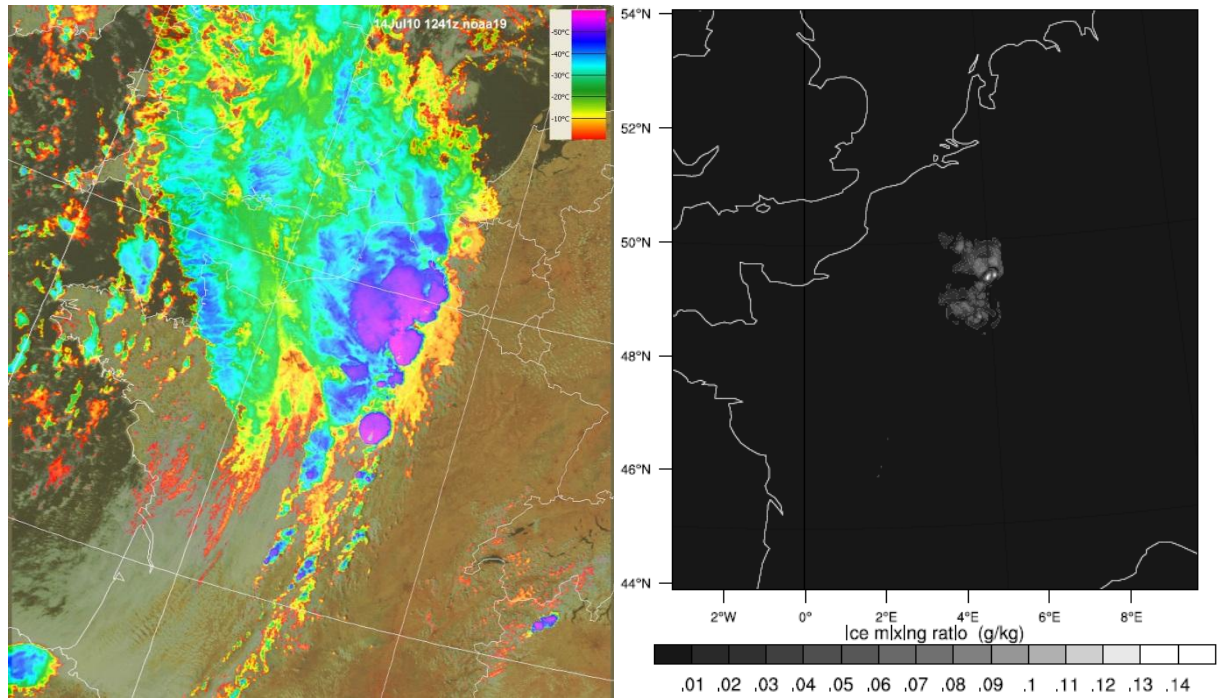
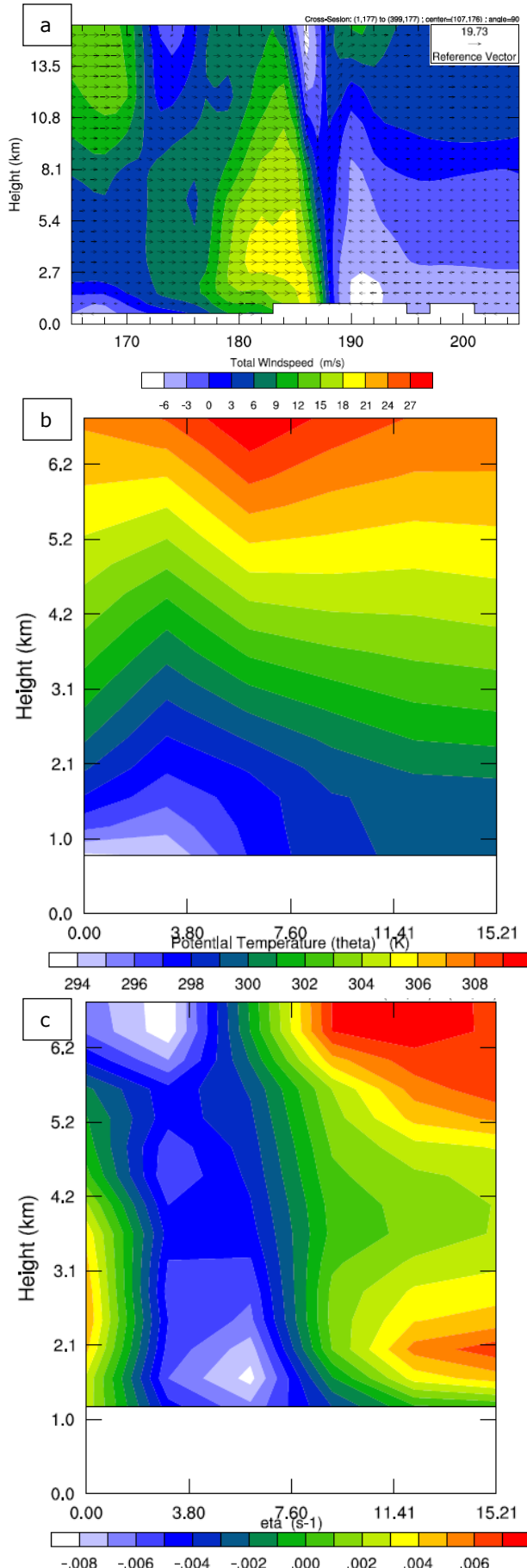


Fig. 16: Meteosat HRPT satellite image (left, EUMETSAT 2010b) for 14 July 2010, 12:41 UTC compared with the ice mixing ratio (right) at eta level 25 (approx. 13000m) for 14 July 2010, 12:00 UTC.

For the analysis with ice particles, there is a great difference between certain model simulations. This is caused by the moisture scheme, since WSM6 includes graupel and ice, while WSM3 does not. This means that the WSM3 model output cannot contain analysis for ice at any altitude, since it is not generated by the model.



4.3 Dynamical performance

In this section we describe the dynamical performance as proposed in section 3.2.3. We focus on the early-mid stage (8:00 UTC - 9:00 UTC), the mid-stage (12:00 UTC) and the end stage (16:00 UTC).

4.3.1 Early-mid stage

As the theory explained in section 2.1 predicted, relatively warm, moist air causes, due to lifting, caused the first rain over Western France, near the city of Le Mans. This rain will form the early beginnings of a (shallow) cold pool. This shallow cold pool and associated rain is visible in Fig. 18 inside the red circle. To better understand the model performance and to see whether or not WRF also follows the RKW-theory a cross-section (with Le Mans as pivot point) has been made for wind speed, potential temperature and vorticity and is visible in Fig. 17.

The stage described here has, despite being so early in the day (10:00 local time), already past the early stage of the storm development described by the RKW-theory. This is due to the already formed cold pool, with the leading edge around 7.60 km, which is visible in Fig. 17b.

At first look, a similar pattern as Fig. 6d can be seen in this figure. There is a clear zone with upward moving air near grid point 188. On the right hand side of this zone, a zone with wind shear (white to light blue) is visible near the surface indicating a similar pattern as in Fig. 6d with decreasing wind with altitude, resulting in a positive vorticity. Higher up in the figure another clear example of positive vorticity can be seen, since the wind is turning from a negative to positive value with increasing height. This is also visible from the vorticity plot of Fig. 17c. On the left hand side, we expect a zone throughout the cross-section with negative vorticity counteracting the positive vorticity. This zone is visible, resulting in the upstream flow at the boundaries ($\eta = 0$) of the vorticity. Although there is a clear difference, with the RKW theory, at the top of the figure where the upstream flow splits (around 9 km height) and forms a secondary upstream flow. Also, the upstream flow is tilted slightly to the left, which tells us that the cold pool associated vorticity is stronger than the wind shear vorticity at this particular moment. Therefore, Fig. 17 does not show the most ideal case, according the RKW theory, for storm development. However, because the upstream flow region is nearly vertical, we expect the storm to grow in magnitude during the next few hours.

Fig. 17: Top, cross-section (x-axes are grid points, approx. 2.5km) of the horizontal wind velocity (shaded, m/s) and its interaction with vertical velocity (curved arrows, m/s) with the pivot point of Le Mans, France under an angle of 90 degrees (E-W orientation). Middle, cross-section of the potential temperature around the cold pool edge. Bottom, cross-section of the vorticity around the cold pool edge. All at 9:00 UTC, 14 July 2010.

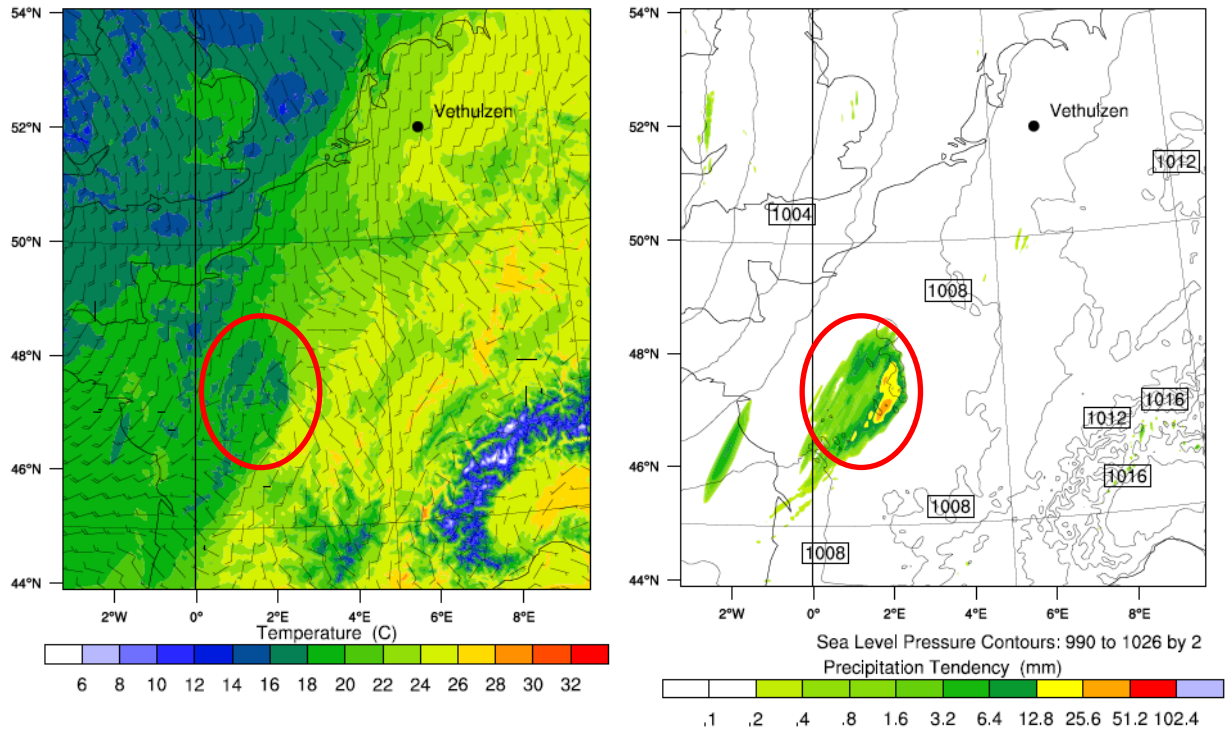


Fig. 18: An overview of the wind (barbs, kts) and temperature (left) and cumulative precipitation over the last hour and sea level pressure (right) for 14 July 2010, 8:00UTC for the entire domain. The red circle marks the area where the shallow cold pool has developed.

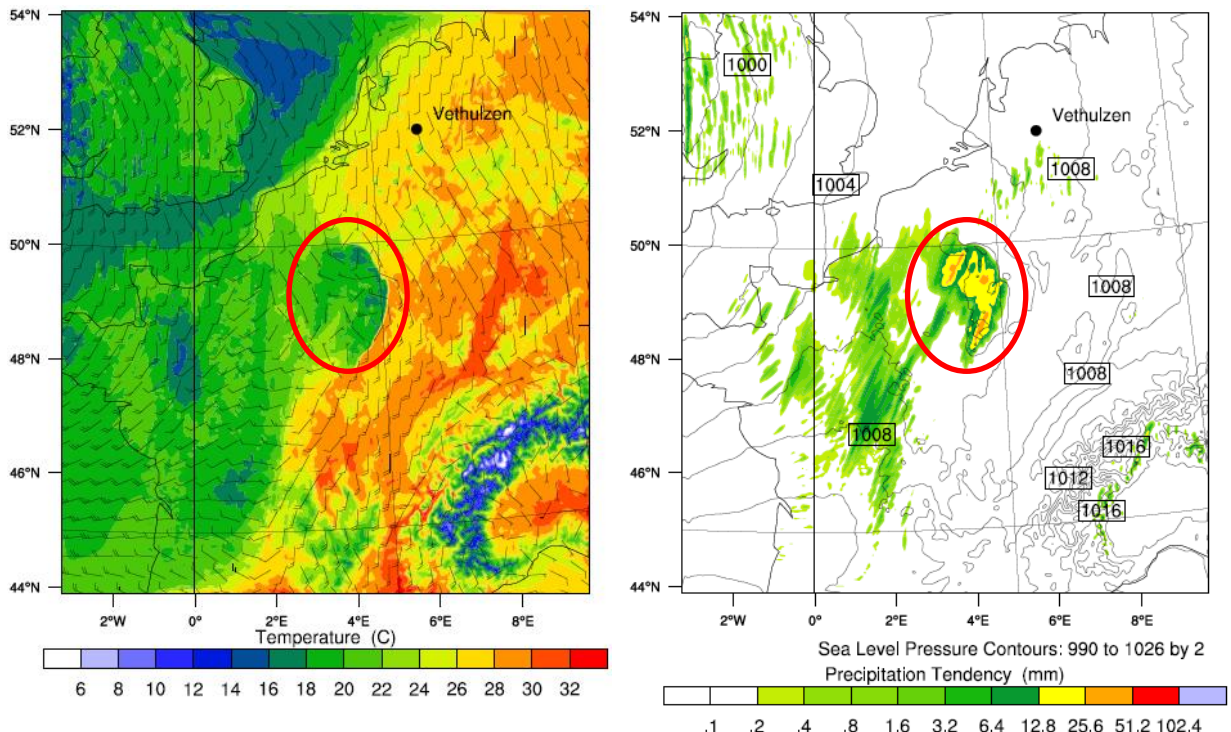


Fig. 19: An overview of the wind (barbs, kts) and temperature (left) and cumulative precipitation over the last hour and sea level pressure (right) for 14 July 2010, 12:00UTC for the entire domain. The red circle marks the area where the cold pool is present.

4.3.2 Mid stage

The cold pool, visible inside the red circle of Fig. 19, moved from the Western part to the Northern part of France and, as predicted, increased in strength (temperature difference between the cold pool and its direct environment increased) and is now near the city of Châlons-en-Champagne. The growth of the cold pool is not only visible in the horizontal, but also in the vertical, which is visible in Fig. 17. The potential temperature decreased only by 1°C , but the gradient in the vertical is more steep, reflected in a decrease in distance between the isotherms. Also, the leading edge of the cold pool is more developed and therefore better visible. We also see an increase in precipitation, the zone till 25.6 mm/hr (yellow) grew in size and more and bigger 51.2 mm/hr (orange) spots are visible within the red circle (Fig. 19).

In order to still have a developing storm cell, the increasing magnitude of the cold pool needs to be matched by an increasing wind shear vorticity. This can be seen in Fig. 20a. Compared with the early-mid stage, we see an increase in wind on the right side of the cold pools leading edge (marked by the white-blue colours), indicating a further increase in vorticity associated with shear on the right side. The updraft flow is also still clearly visible and widened compared with Fig. 17. Also the splitting of the updraft flow, as was shown in Fig. 17, is no longer visible, indicating a more developed updraft profile.

Besides an increase in wind speed on the right side of the profile, on the left side we see a formation of a rear-inflow jet, indicated by the relatively high windspeed at gridcell 330 at approximately 5.4 km (red colours, Fig. 20a). This is confirmed by the RKW theory. However the generated rear-inflow jet does not lead to a more erect lower profile, in this particular case. There is no change in the obliquity of the vertical updraft over the entire profile, excluding any evidence of the rear-inflow jet influencing the vertical updraft profile. What we also can conclude from Fig. 20 is, and this in contrast to Fig. 17, that the vertical wind speed increases with height, reaching a maximum (15-20 m/s) at the top of the wind profile (~ 15 km) in the middle of the updraft flow. Therefore we can say that the moisture associated with this updraft is penetrating through the tropopause, since the tropopause is not known to reach the altitude of 15 km in the Western Europe, which indicates a very severe storm development. Because the vertical velocity of this storm is high enough to reach the tropopause (and probably spreads along the tropopause), we conclude that storm will continue to grow.

Looking at the vorticity in Fig. 20c we can see a clear negative area around 5.3 km and a clear positive area near the surface of the profile. The vorticity described above is generated by the rear-inflow jet, because equation 2 states that the vorticity is at its minimum where the windspeed decrease in height is at its maximum. Since the peak of the velocity associated with the rear-inflow jet, we expect the sharpest decrease in windspeed with height here, meaning that we would see a minimum of the vorticity near the maximum of the windspeed. In this case, the maximum of the windspeed is around 5.3 km. However, because of the interval of the colours of Fig. 20a, it is not possible to conclude this by looking at the figure alone. The interval is too broad.

Looking at the overall vorticity, we conclude that for this case the vorticity associated with the rear-inflow jet dominates the vorticity generated by shear or buoyancy and therefore the pattern visible in Fig. 10b, besides the rear-inflow vorticity is not shown in Fig. 20, due to the relatively high wind speeds of the rear-inflow jet.

4.3.3 End stage

We see that the storm moved further North and at 16:00 UTC has already passed Vethuizen, meaning that maxima of precipitation are also North of Vethuizen. This is not including the small spots of high precipitation, which are not associated with the storm, in the province of Zeeland (Fig. 22). We also see a sharp temperature gradient North of Vethuizen, which is in the same order of magnitude as at 12:00 UTC ($\sim 10^{\circ}\text{C}$). We would expect the storm to be in the same order of magnitude as at 12:00, if the vorticity associated with wind shear is still in a balance with the cold pool vorticity. Therefore we look at the cross sections, which are visible in Fig. 21.

We notice the lack of a clear updraft flow, which indicates that the updraft flow has been severely weakened and almost disappeared. The wind speed throughout the profile is now directed in the direction of storm movement and therefore not optimal for storm growth. This stage indicates the end stage of the storm. This is confirmed by looking at the cold pool. Despite the same temperature differences, as concluded above, we see a broader cold pool boundary, indicating that also the cold pool has, although slightly, decreased in magnitude in both its vertical and horizontal extent.

Still visible in the wind cross section is the rear-inflow jet. The jet decreased in magnitude, but still has a great influence on the general pattern. This is best shown by looking at the vorticity of Fig. 21c. The vorticity associated with the rear-inflow jet still dominates the profile, would be expected, since the general wind speed and buoyancy decreased. If we compare this vorticity figure with the Fig. 8a, we see that at the leading edge of the cold pool the vorticity is negative. Above the cold pool and the rear-inflow

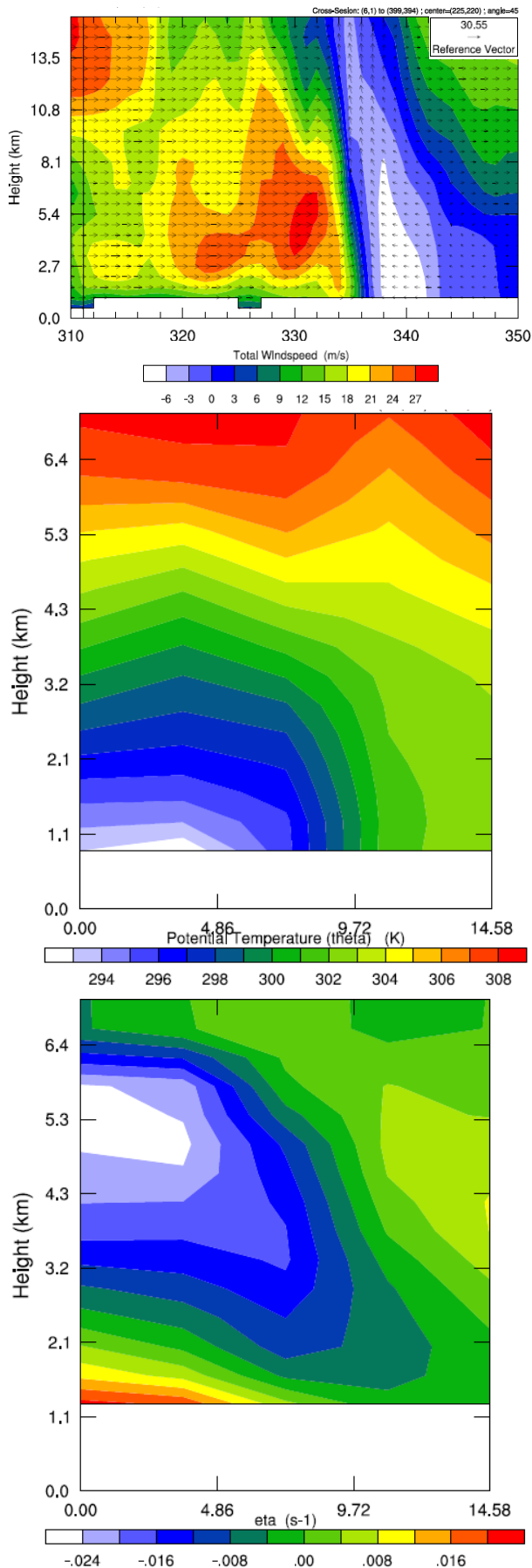


Fig.20: Top, cross-section (x-axes are grid points, approx. 2.5km) of the horizontal wind velocity (shaded, m/s) and its interaction with vertical velocity (curved arrows, m/s) with the pivot point of Châlons-en-Champagne, France under an angle of 45 degrees (SE-NW orientation). Middle, cross-section of the potential temperature around the cold pool edge. Bottom, cross-section of the vorticity around the cold pool edge. All at 12:00 UTC, 14 July 2010.

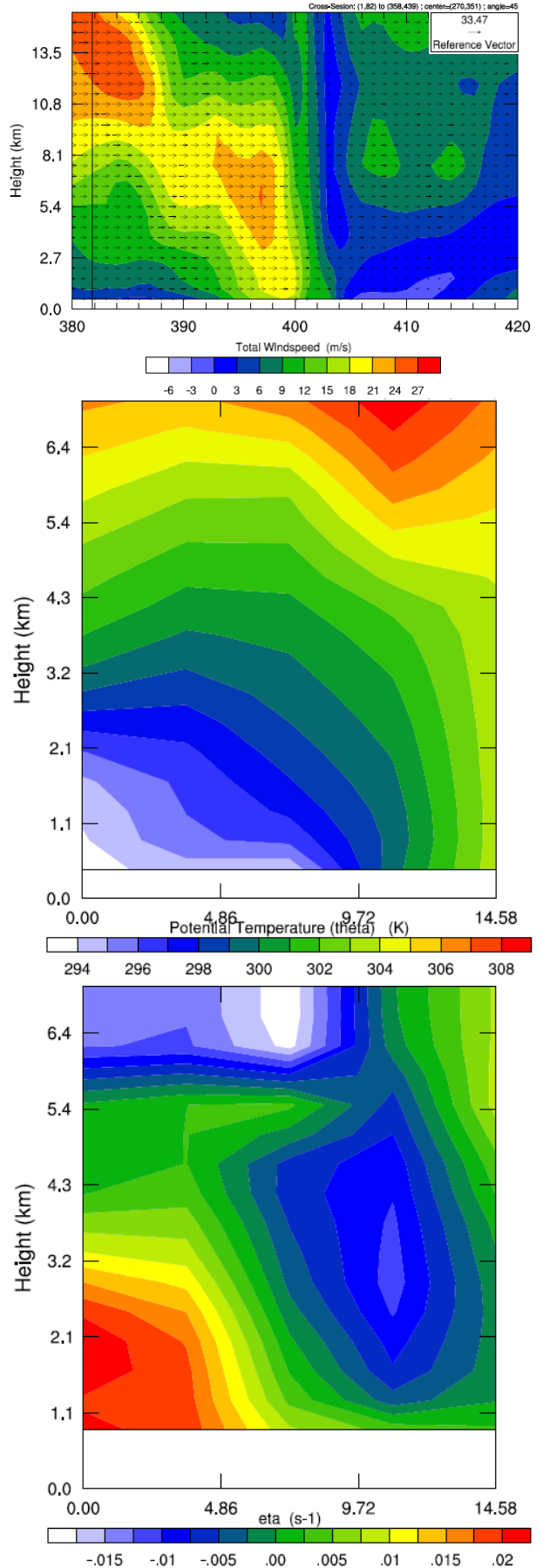


Fig. 21: Top, cross-section (x-axes are grid points, approx. 2.5km) of the horizontal wind velocity (shaded, m/s) and its interaction with vertical velocity (curved arrows, m/s) with the pivot point of Vethuizen, Netherlands under an angle of 45 degrees (SE-NW orientation). Middle, cross-section of the potential temperature around the cold pool edge. Bottom, cross-section of the vorticity around the cold pool edge. All at 16:00 UTC, 14 July 2010.

jet, the vorticity is also negative and near the end of the cold pool (right side) the vorticity is positive. All these patterns are also visible in this figure. Although the vorticity figure of Fig. 21c shows more similarity with Fig. 10b, which is caused by the relatively strong rear-inflow jet at 16:00 UTC.

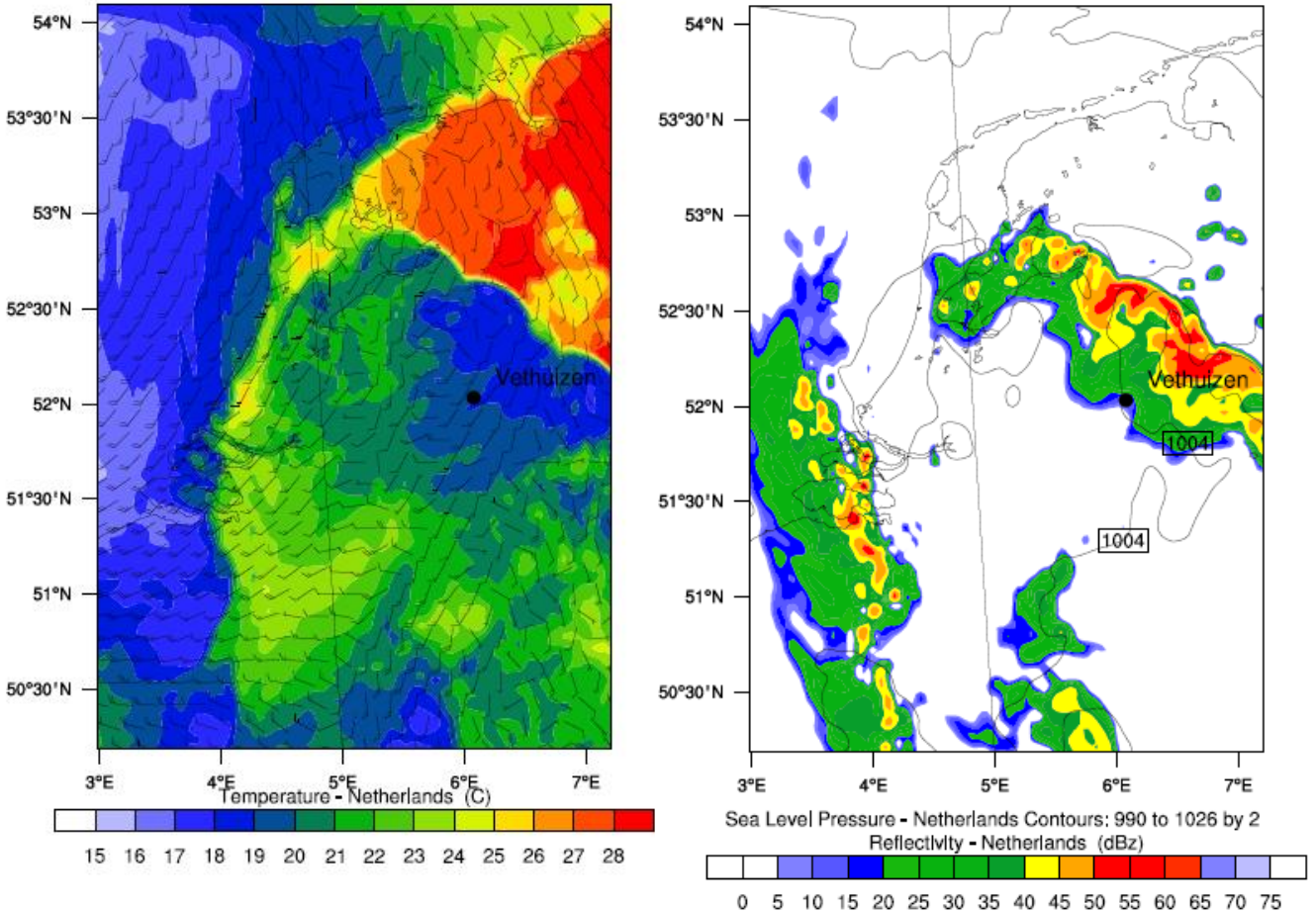


Fig. 22: An overview of the wind (barbs, kts) and temperature (left) and reflectivity and sea level pressure (right) for 14 July 2010, 12:00UTC for the Netherlands.

4.4 RKW-theory Balance

4.4.1 Storm motion

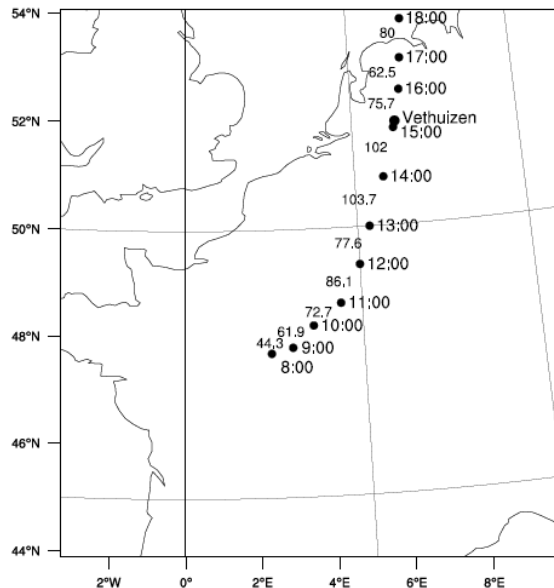


Fig. 23: The track and propagation speed of the storm depicted by the WRF model output. The dots represent the location at a certain time (right of the location) and the speed of the storm (km/h, between the dots over which the speed is measured).

Important for the RKW-theory balance is the storm motion, since the RKW-theory does not clearly state whether or not the wind speed is taken with or without storm relative motion, despite the importance of the wind speed for the balance equation. Therefore in this analysis both states are described. The storm motion can be seen in Fig. 23.

Fig. 23 shows an increasing storm translation over time (excluding the motion between 12:00 and 13:00 UTC) till the storm reaches its maximum near Vethuizen (around 15:00 UTC). When the storm has reached its maximum intensity, we see a drop in the storm motion, indicating a drop in intensity. Also, we can see a shift in the direction of the propagation speed of the system. Going from an East-North-East direction in Central France, to an almost Northward direction over the Netherlands and the North Sea.

4.4.2 RKW-theory tendency

As described in section 2.5.1, we look at the balance equation (equation 5), which illustrates all the processes included in the theory. The different terms of the balance equation can be seen in Fig. 24. Where

$F_1 = \int_0^d (B_L - B_R) dz$	Buoyancy
$F_2 = \int_0^d (u\eta)_L dz$	Flux left
$F_3 = \int_L^R (w\eta)_d dx$	Flux top
$F_4 = 0$	Flux bottom
$F_5 = \int_0^d (u\eta)_R dz$	Flux right

In order to calculate the values associated with these processes we need to rewrite the formulas to:

$F_1 = \sum_{i=0}^d (B_{L,i} - B_{R,i}) \cdot d_i$	Buoyancy
$F_2 = \sum_{i=0}^d (u\eta)_{L,i} \cdot d_i$	Flux left
$F_3 = \sum_{i=L}^R (w\eta)_{d,i} \cdot x_i$	Flux top
$F_4 = 0$	Flux bottom
$F_5 = \sum_{i=0}^d (u\eta)_{R,i} \cdot d_i$	Flux right

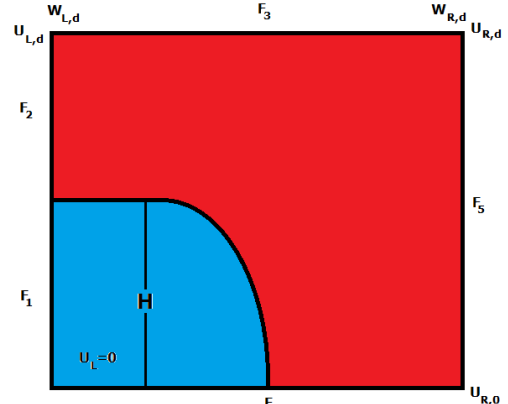


Fig. 24: Overview of the different terms in the balance equation.

Where, d_i is the depth of layer i and x_i is the width of layer i . The balance of these terms will give the tendency as described in the balance equation.

For the tendency we look at two runs, the MYJ + WSM3 and the YSU + WSM6, due to their performance on temperature and pressure, but also since the parameterization schemes show the greatest internal difference. The outcome of the analysis for both runs and both with and without taking the storm motion into account can be seen in Table 3 and Table 4.

Table 3: An overview of the contribution of the different terms ($m^2 s^{-2}$) of the balance equation of the RKW-theory for the three different stages, start (9:00 UTC), middle (12:00 UTC) and end (16:00 UTC).

	MYJ + WSM3			YSU + WSM6		
	start	mid	end	start	mid	end
F1	0.23277	0.26750	0.25670	0.16080	0.30930	0.31242
F2	-0.17202	-0.03624	-0.81047	-0.32414	-0.00745	-3.14094
F3	-0.00085	-0.02696	-0.00135	-0.02734	-0.00303	-0.00930
F4	0	0	0	0	0	0
F5	0.00211	0.04980	1.86750	-0.02216	0.04117	0.14252
Balance	0.0595	0.2084	-2.4199	-0.1138	0.2637	-2.9617

Table 4: An overview of the contribution of the different terms ($m^2 s^{-2}$) of the balance equation of the RKW-theory for the three different stages, start (9:00 UTC), middle (12:00 UTC) and end (16:00 UTC) with the storm motion taken into account.

	MYJ + WSM3			YSU + WSM6		
	start	mid	end	start	mid	end
motion [m/s]	12.3	23.9	21.0	12.3	23.9	21.0
F1	0.23277	0.26750	0.25670	0.16080	0.30930	0.31242
F2	-0.71376	0.46143	-0.09828	-0.02082	0.54481	-0.33873
F3	-0.00085	-0.02696	-0.00135	-0.02734	-0.00303	-0.00930
F4	0	0	0	0	0	0
F5	-0.23754	-0.53008	-0.63562	-0.31130	-0.11210	-0.09098
Balance	-0.2426	1.2860	0.7954	0.4786	0.9692	0.0740

Table 3 and Table 4 show the importance of the different terms on the balance equation. Clearly visible is the minor influence of the vertical shear flux (F_3) on the balance equation. In comparison with the largest contributing term, the vertical shear varies from 0.1% to 8.8% of the largest contributing term, concluding that the vertical shear has little importance for the balance equation.

We also see an increase in buoyancy (F_1) between the start and middle phase. This may indicate an increasing temperature difference in the vertical or in the horizontal (difference between the left and right boundary). For the YSU + WSM6 run we see that the buoyancy even further increases with time,

although into a lesser degree as between the start and middle phase, which can be explained by a still increasing cold pool. The difference between the MYJ + WSM3 run and the YSU + WSM6 run can be explained by the relatively colder cold pool ($\sim 0.5^\circ\text{C}$) and warmer surroundings ($\sim 2.0^\circ\text{C}$) for the YSU + WSM6 run.

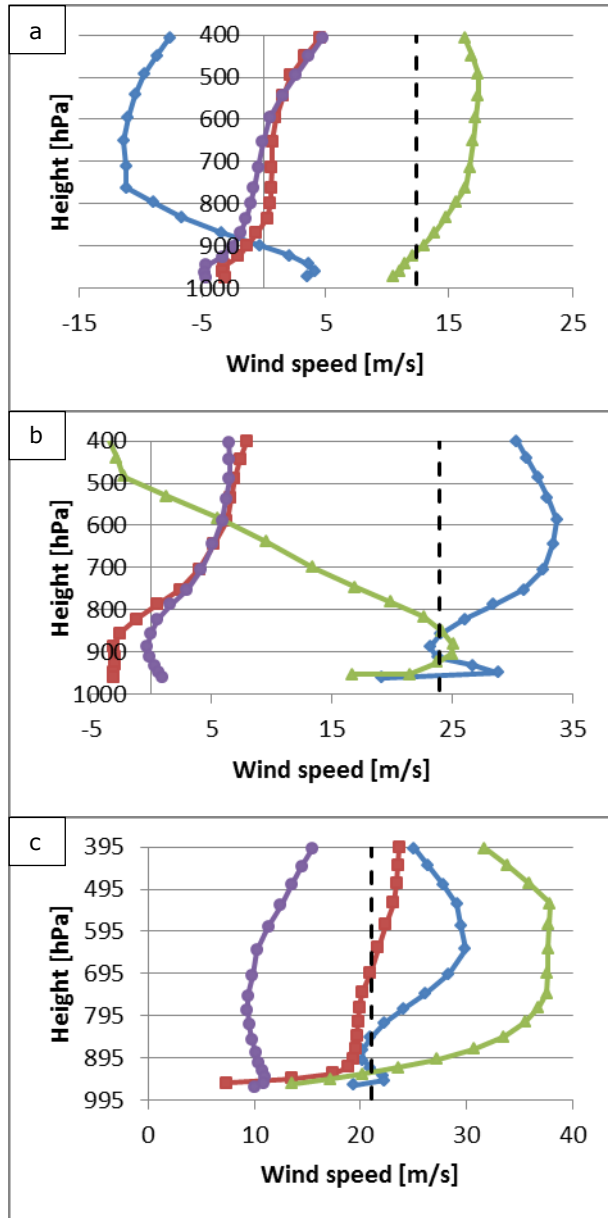


Fig. 25: Vertical profile of the wind speed with the storm motion (black dashed line) for start (a, 9:00), mid (b, 12:00) and end (c, 16:00), with MYJ+WSM3 left (blue), MYJ+WSM3 right (red), YSU+WSM6 left (green) and YSU+WSM6 right (purple).

YSU+WSM6, since we subtract the storm relative motion, the wind speed is lower, which also lowers the fluxes.

4.4.3 RKW-theory assumptions

The balance equation is based upon some assumptions. As stated in section 2.3.1, the theory assumes a steady state, resulting in a balance of 0. If we look at Table 3 and 4, we clearly see that there is no steady state. If we compare the balance with the highest contributing term we see that the end balance is in some cases greater than the highest contributing term (i.e. MYJ+WSM3 end), so we can therefore, for these simulations, not assume a balance and state that there is a steady state or near steady state like the RKW-theory suggests.

The wind shear flux, both left (F_2) and right (F_5), is highly variable and varies from -3.14094 to $0.54481 \text{ m}^2 \text{ s}^{-2}$ for the left flux and varies from -0.63562 to $1.86750 \text{ m}^2 \text{ s}^{-2}$ for the right flux. We can see that for the normal overview the left flux is dominated by negative values, while the right flux is mainly positive. For the storm motion overview, we see that the right flux is dominated by negative values, while the left flux has positive values in the mid stage, but negative values at the start and end stage.

The high variation can be explained by the vertical wind profile (Fig. 25). The wind profiles of both (MYJ+WSM3 and YSU+WSM6) right sides in the start and mid stage are similar (red and purple line in Fig. 25). The left side for both runs show great differences for all runs, mainly in the upper part of the profile. In the early stage we see relatively high wind speeds throughout the profile for YSU+WSM6 (green), while the MYJ+WSM3 (blue) starts with a positive wind speed, but rapidly shifts direction and speed in the vertical. The profile of the mid stage starts similar, although the MYJ+WSM3 shows some kind of surface jet, but higher in altitude we see a decline in wind speed for the YSU+WSM6 run. The wind speed for the MYJ+WSM3 run is relatively high, with a maximum wind speed of 33.7 m s^{-1} at 587 hPa. For the end stage, the right sides are clearly different. The pattern however is somewhat similar, but there is a difference around 10 m s^{-1} at almost every point in the profile, with YSU+WSM6 as the profile with the lower wind speeds. For the left side it is mirrored. We see a somewhat similar pattern with a difference around 10 m s^{-1} throughout the profile, but now the YSU+WSM6 is the run with the higher wind speeds, which has a maximum of 37.9 m s^{-1} at 528 hPa. For the YSU+WSM6 left, we also notice a great wind increase in the lower part of the profile, indicating a relatively large wind shear. A large wind shear and large wind speed result in a relatively large flux, which explains the large negative value of F_2 at the end stage for YSU+WSM6 ($-3.14 \text{ m}^2 \text{ s}^{-2}$). If we compare the regular results with the results of the storm relative motion, we see that the values of F_2 and F_5 are relatively lower. This is explained in the same way as the large negative value of

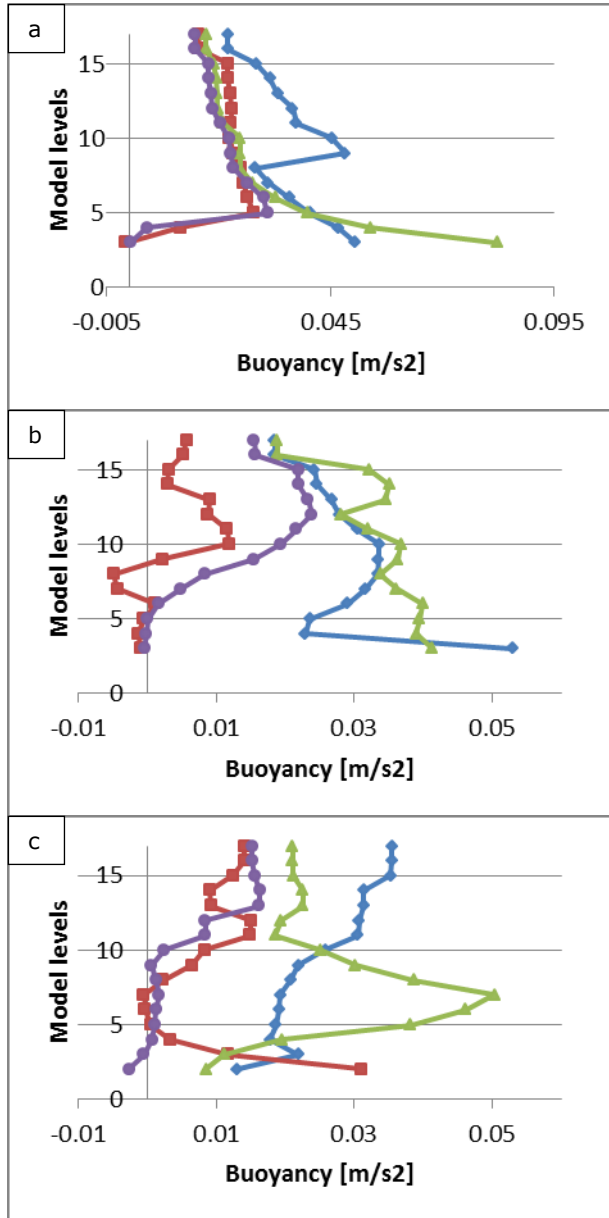


Fig. 26: Vertical buoyancy profile with model levels on the y-axis and for start (a, 9:00), mid (b, 12:00) and end (c, 16:00), with MYJ+WSM3 left (blue), MYJ+WSM3 right (red), YSU+WSM6 left (green) and YSU+WSM6 right (purple).

previous section, the flux at the top is relatively small compared with the other fluxes and can therefore be neglected. The reason behind the low fluxes can be explained by the vertical wind profile (w) and the corresponding flux (vertical shear, dw/dx), which are visible in Fig. 27. Fig. 27a shows for the vertical wind an evenly distributed profile, with a maximum in the upper middle part of the figure. A schematic picture of this situation is shown in Fig. 28a. Because the wind is evenly distributed, we see a maximum in the vertical shear left of the maximum of the vertical wind and a minimum in the vertical shear right of the maximum of the vertical wind. The minimum in the vertical shear has almost the same order of magnitude, although negative, as the maximum in the vertical shear. If we would multiply the vertical wind with the vertical shear, creating the flux, and integrate it over the profile, we get Fig. 27b and its schematic counterpart Fig. 28b. Looking mainly at Fig. 28b, we can understand that the effect of the vertical wind shear is very small on the total balance. This is because the area under the curve ($\int_L^R w\eta dx$) will counteract each other and are in the same order of magnitude (blue and red area of Fig. 28b). Therefore we conclude that the result of the rigid plate is justified ($w\eta = 0$), but the rigid plate principle does not describe the situation well.

The RKW theory also assumes that the wind in the cold pool itself is stagnant, $U_{L,0} = 0$. Looking at YSU+WSM6 right (green) and MYJ+WSM3 right (blue) wind profile of Fig. 25, we see that the wind in the lower part of the profile is not stagnant. Although, if we take the storm relative motion into account, we see that the lowest point of the wind profile is relatively near the storm motion line. However the deviations between the storm motion line and the wind profile are ranging between 0.8 to 8.8 m/s. Also we see some jet formations (especially for the MYJ+WSM3 run) relatively low in the profile, concluding that the wind is not stagnant in this section. This conclusion may be different when we do a countless number of runs. Since we are only looking at 6 different runs for the same storm, the results may be completely different for another storm, with the same overall patterns, which are not checked in this paper.

Fig. 26 shows the vertical buoyancy profile. The RKW-theory states that the buoyancy is limited to the bottom part of the profile, till the boundary layer is reached, and accounted only for the left part. Fig. 26 clearly shows that the buoyancy is dominated by the left side, this is due the relatively large potential temperature differences, in height, of the cold pool. Looking at the first stage, we see that the large temperature difference is present in the lowest levels of the profile, reaching almost equal values of buoyancy between left and right around level 7 (approximately 1300m), which is equal to the boundary layer height in this case. We also see that if we only take the left part into account, and not subtract left with right, we overestimate the total buoyancy around 40-50%. In the mid and end stage, we see that, especially the end stage of the YSU+WSM6 run, the right side the buoyancy is near zero for the lower part of the profile. This means that the lower layer of the atmosphere is well mixed and (almost) homogeneous in potential temperature. So the assumption of RKW is based upon a perfectly mixed boundary layer on the right side, which is not the case for our model simulations.

The last assumption made by RKW is a rigid plate at $z = d$ resulting in a $w\eta = 0$. As we stated in our previous section, the flux at the top is relatively small compared with the other fluxes and can therefore be neglected. The reason behind the low fluxes can be explained by the vertical wind profile (w) and the corresponding flux (vertical shear, dw/dx), which are visible in Fig. 27. Fig. 27a shows for the vertical wind an evenly distributed profile, with a maximum in the upper middle part of the figure. A schematic picture of this situation is shown in Fig. 28a. Because the wind is evenly distributed, we see a maximum in the vertical shear left of the maximum of the vertical wind and a minimum in the vertical shear right of the maximum of the vertical wind. The minimum in the vertical shear has almost the same order of magnitude, although negative, as the maximum in the vertical shear. If we would multiply the vertical wind with the vertical shear, creating the flux, and integrate it over the profile, we get Fig. 27b and its schematic counterpart Fig. 28b. Looking mainly at Fig. 28b, we can understand that the effect of the vertical wind shear is very small on the total balance. This is because the area under the curve ($\int_L^R w\eta dx$) will counteract each other and are in the same order of magnitude (blue and red area of Fig. 28b).

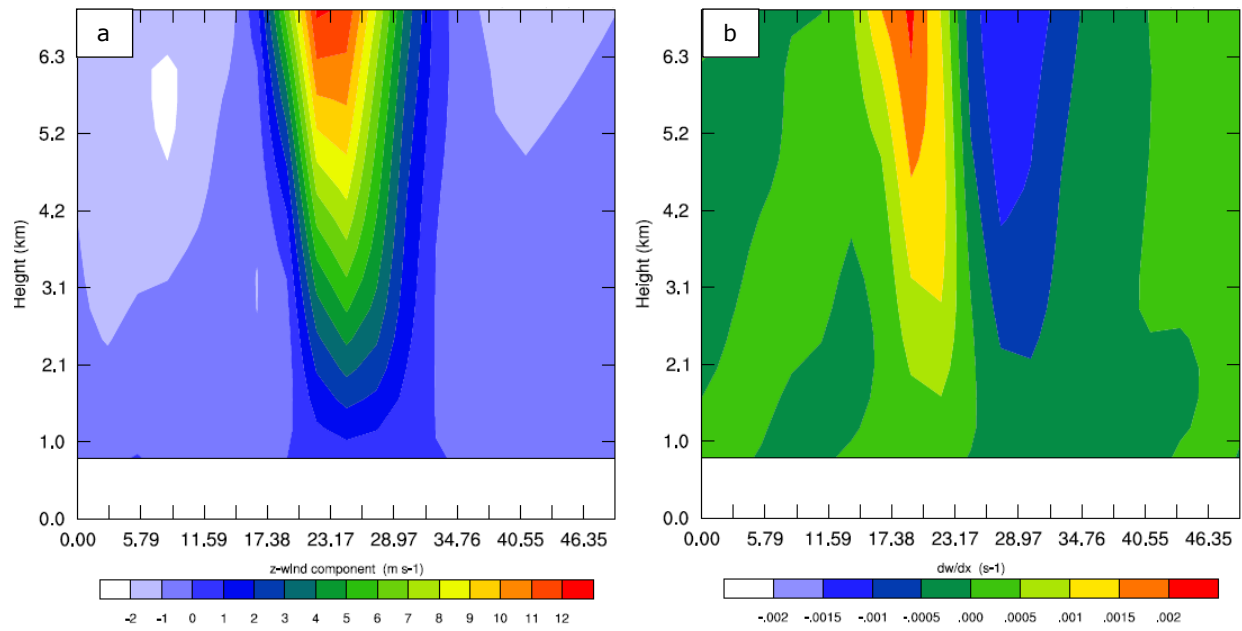


Fig. 27: Vertical profiles of a) vertical velocity (w) and b) the corresponding flux (dw/dx).

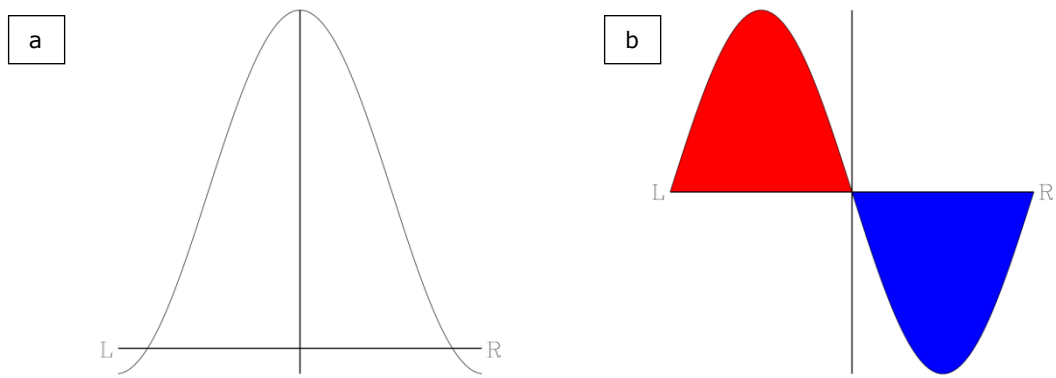


Fig. 28: Schematic overview of, a) the vertical velocity (w) at the top of Fig. 27 and b) the corresponding flux (dw/dx) at the top of Fig. 27 with the red colours indicating positive flux and the blue colours indicating a negative flux.

5. Conclusions and future recommendations

This research project focused on the dynamics and the performance with the WRF model of the squall line of 14 July over the Netherlands, which peaked in intensity over Vethuizen. Despite alterations in choosing the parameterization schemes, all runs predicted the storm to pass Vethuizen between 1.5 – 3 hours too early. The reason for the early pass is unknown and therefore we could not compare our results with Van Dijke et al. 2010. We tested it with a smaller geospatial resolution or a smoother build up of the vertical resolution, but these runs showed no improvement. Also, choosing a different parameterization scheme had no great influence on the model output, all runs performed similar (Appendices E, F and G), although looking at the five statistical performance checks for temperature and pressure, the YSU+WSM6 run performed overall the best, which can be explained mainly by the timing of the cold pool passage. YSU+WSM6 was the run which was closest to the exact timing of passage of the system.

Furthermore, the RKW theory explained us more about the different development stages of a (generalised) thunderstorm. After looking at the output we conclude that the overall visual dynamics (i.e. vertical updrafts, vorticity location, rear-inflow jet position) are well represented. Since there are no numbers available for the strength of each of these processes, we cannot tell whether or not WRF performs well looking at the order of magnitude.

The assumptions of the RKW-theory, stated by Rotunno, Klemp and Weisman in their work, are not all justified. Starting from the balance equation to equation 9 ($c=\Delta u$), they assumed: a steady balance, stagnant air in the cold pool, buoyancy limited within the boundary layer, no buoyancy at the warm side and a rigid plate principle at the top of their model.

A (near-) steady state was almost never present in our runs. In only 2 of the 12 cases described a balance near zero. In all the other cases the end balance is almost equal or even exceeding the magnitude of the largest contributing term.

Looking at both regular motion and storm relative motion, we see that there is no stagnant air in the cold pool itself. It varies from $+5 \text{ m s}^{-1}$ to -10 m s^{-1} in the mid stage alone.

The buoyancy is driven by temperature gradients and these are largest in the cold pool, within the boundary layer, but not exclusive to the cold pool. This means that there is buoyancy above the cold pool and right of the leading edge of the cold pool, making this assumption inconclusive. We therefore say that the buoyancy term described in the balance equation (integrating the difference between the buoyancy left and the buoyancy right over the entire profile) is a better approximation.

Lastly, the rigid plate principle at the top does not describe the situation well. There are particles flowing through the rigid plate. However its result ($w\eta = 0$) is well represented. This is caused by a symmetrical maximum in vertical velocity, which in the end results in a positive flux right of the maximum and a negative flux left of the maximum vertical velocity. Because the maximum and minimum are in the same order of magnitude, integrating from left to right results in a total area which is (near-) 0. The updraft generated vorticity flux can therefore be neglected.

We see that all 5 assumptions are not completely justified, however in many of the assumptions the result, sometimes with another approach as Rotunno, Klemp and Weisman stated in their paper, are at least partially in this analysis. This may explain why the general pattern of the visual dynamics are well represented.

For this particular case we see that the model follows the theory well, however we do not know how the model performs in other cases. Also this case describes a very regional situation, it is therefore recommended to look at squall lines outside Western Europe (e.g. United States or Central Europe), to see whether or not WRF still follows the theory. Also, typical storms of this magnitude form in tens-of-minutes, so while looking at hourly snapshots, you may miss some of the details. The same goes for the horizontal and vertical grid. These processes happen on a kilometre scale, so the 2.5 by 2.5 kilometre grid may miss some of the details as well. Recommended is to make use of nested domains, preferably a nested domain that moves with the thermal low that originates from Central France. In this way you can model certain parts of the domain more detailed and may give better results. In the vertical we can also add more points in order to get a more detailed updraft, especially near the surface and near the top of the model.

Acknowledgements

I would like to thank my supervisor Dr. Leo Kroon for his guidance and help, with the evaluation of my draft versions, answering my questions, motivating me and keeping me to a general structure during the project. I would like to thank Dr. Reinder Ronda and Dr. Gert-Jan Steeneveld with their help starting up and working with the WRF model, Dr. Hidde Leijnse from the KNMI for the radar data and analysis of this data, Daniël van Dijke with his help trying to get better WRF results and lastly I would like to thank Liduin Burgering for her mental support as well as her knowledge of and help with the ncl scripts I used to get my results.

Literature references

Bryan, G.H. 2012. What is RKW Theory?. Handouts of the 26th Conference on Severe Local Storms.

Corfidi, S.F. 2003. Cold Pools and MCS Propagation: Forecasting the Motion of Downwind-Developing MCSs. *Weather and Forecasting*, **18**:12, 997-1017.

Van Delden, A. 2001. The synoptic setting of thunderstorms in western Europe. *Atmospheric Research*, **56**, 89-110.

Van Dijke, D., Y. Hinssen and F. Bijlsma, 2010. *A 500m WRF hindcast of a microburst event in The Netherlands*. Meteo Group, MeteoConsult.

Dudhia, J., S.Y. Hong, and K.S. Lim, 2008: A new method for representing mixed-phase particle fall speeds in bulk microphysics parameterizations. *J. Met. Soc. Japan*, in press.

Dudhia, J., 2010. *Microphysics options in WRF*. NCAR/MMM.

ESA, 2012. *Meteosat second generation*. www.esa.int/Our_Activities/Observing_the_Earth/Meteosat_Second_generation/MSG_overview2 (accessed on 24-4-2014)

FMI, 2014. Convective Cloud Features in Typical Synoptic Environments: The Spanish Plume – Meteorological Physical Background. *FMI*. <http://rammb.cira.colostate.edu/wmvl/vrl/tutorials/satmanu-eumetsat/satmanu/cms/spl/backgr.htm> (accessed on 13-3-2014)

Fujita, T. T., 1981. Tornadoes and Downbursts in the Context of Generalized Planetary Scales. *J. Atmos. Sci.*, **38**, 1511-1534.

Groenland R., J. Hemink, J. Kuiper, N. Wever and G. Groen, 2010. Het noodweer van juli 2010 in Vethuizen en Neerkant e.o., meteorologisch onderzoek en achtergronden. *KNMI publication*.

Hamid, K. and Delobbe, L., 2007. F3-Tornado in Belgium. *Preprints, 4th European Conf. on Severe Storms, Trieste*.

Hamid, K., 2012. Investigation of the passage of a derecho in Belgium. *Atmospheric Research*, **107**, 86-105.

Hong, S.Y., J. Dudhia, and S.H. Chen, 2004: A Revised Approach to Ice Microphysical Processes for the Bulk Parameterization of Clouds and Precipitation, *Mon. Wea. Rev.*, **132**, 103-120.

Hu, X. M., Nielsen-Gammon, J. W. and Zhang, F., 2010. Evaluation of Planetary Boundary Layer Schemes in the WRF Model. *Journal of Applied Meteorology and Climatology*, **49**, 1831-1844.

KNMI, 2010. Vooral valwinden bij noodweer 14 juli. *KNMI nieuwsoverzicht*. http://www.knmi.nl/cms/content/82661/vooral_valwinden_bij_noodweer_14_juli (accessed on 5-6-2013)

Lemone, M.A., M. Tewari, F. Chen and J. Dudhia, 2012. Determined Fair-Weather CBL Depths in the ARW-WRF Model and Their Comparison to CASES-97 Observations. *Monthly Weather Review*, **141**:1, 30-54.

Michalakes, J., J. Dudhia, D. Gill, J. Klemp and W. Skamarock, 1998. Design of a next-generation regional weather research and forecast model. **Towards Teracomputing**, World Scientific, River Edge, New Jersey. 117-124.

Michalakes, J., J. Dudhia, D. Gill, T. Henderson, J. Klemp, W. Skamarock, and W. Wang, 2004: "The Weather Research and Forecast Model: Software Architecture and Performance," *to appear in proceedings of the 11th ECMWF Workshop on the Use of High Performance Computing In Meteorology*, **25-29 October 2004**, Reading U.K. Ed. George Mozdynski.

NOS, 2010. Schade noodweer gisteren 25 miljoen. <http://nos.nl/artikel/172167-schade-noodweer-gisteren-25-miljoen.html> (accessed on 5-6-2013)

Pagowski, M., 2004. Some Comments on PBL Parameterizations in WRF. NOAA Research-Forecast System Laboratory.

Proctor, F. H., 1988. Numerical Simulations of an Isolated Microburst. Part I: Dynamics and Structure. *J. Atmos. Sci.*, **45**, 3137-3160.

Putsay, M., Simon, A., Szenyán, I. and Nagy A. 2012. Pukkelpop Storm, 18-08-2011. *EUMeTrain*. <http://www.eumetrain.org/data/2/274/print.htm>, (accessed on 20-3-2013)

Rotunno, R., J.B. Klemp and M.L. Weisman, 1988. A Theory for Strong, Long-Lived Squall Lines. *Journal of the Atmospheric Sciences*, **45**:3, 463-485.

Skamarock, W.C., Klemp, J.B., Dudhia, J., Gill D.O., Barker, D.M., Duda, M.G., Huang, X., Wang, W. and Powers, J.G., 2008. A Description of the Advanced Research WRF Version 3. NCAR TECHNICAL NOTE. *Mesoscale and Microscale Meteorology Division. National Center for Atmospheric Research Boulder, Colorado, USA*.

Wakimoto, R.M., H.V. Murphy, E.V. Browell and S. Ismail, 2006. The "Triple Point" on 24 May 2002 during IHOP. Part I: Airborne Doppler and LASE Analysis of the Frontal Boundaries and Convection Initiation. *Monthly Weather Review*, **134**:1, 231-250.

Weisman M.L., R. Przybylinski, P. Parrish, W. Schreiber-Abshire, T. Spangler, J. Lamos, S. Jesuroga, J. Syverson and G. Byrd, 1999. The COMET Program. Mesoscale Convective Systems: Squall Lines and Bow Echoes. V3.1. *University Corporation for Atmospheric Research*.

Weisman, M. L., 2001. Bow Echoes: A Tribute to T. T. Fujita. *Bulletin of the American Meteorological Society*, **82**:1, 97-116.

Weisman, M.L. and R. Rutunno, 2004. "A Theory for Strong Long-Lived Squall Lines" Revisited. *Journal of the Atmospheric Sciences*, **61**:4, 361-382.

Weisman, M. L., Davis, C., Wang, W. Manning, K. W. and Klemp, J. B. 2008. Experiences with 0-36-h Explicit Convective Forecasts with the WRF-ARW Model. *Weather and Forecasting*, **23**, 407-437.

Weiss, C.C. and H.B. Bluestein, 2002. Airborne Pseudo-Dual Doppler Analysis of a Druline-Outflow Boundary Intersection. *Monthly Weather Review*, **130**:5, 1207-1225.

Willmott, C.J., 1982. Some Comments on the Evaluation of Model Performance. *Bulletin American Meteorological Society*, **63**:11, 1309-1313.

Wisse, J. S. P. and Vilà-Guerau de Arellano, J., 2004. Analysis of the role of the planetary boundary layer schemes during a severe convective storm. *Annales Geophysicae*, **22**: 1861-1874.

Image references

Front-page photo

KNMI, 2010. Vooral valwinden bij noodweer 14 juli. *KNMI nieuwsoverzicht*. http://www.knmi.nl/cms/content/82661/vooral_valwinden_bij_noodweer_14_juli (accessed on 5-6-2013)

Fig. 2: KNMI, 2013a. *Klimatologie, weerkaarten archief Europa. Analyses vanaf 1 januari 2003 t/m gisteren*. KNMI. <http://www.knmi.nl/klimatologie/daggegevens/weerkaarten/index.cgi> (accessed on 4-9-2013)

Fig. 3: KNMI, 2013b. *Klimatologie, geografische overzichten. Maximum temperatuur*. KNMI. http://www.knmi.nl/klimatologie/geografische_overzichten/archief.cgi (accessed on 5-9-2013)

Fig. 4: FMI, 2014. Convective Cloud Features in Typical Synoptic Environments: The Spanish Plume – Meteorological Physical Background. *FMI*. http://rammb.cira.colostate.edu/wmrvl/tutorials/satmaneu_eumetsat/satmaneu/cms/spl/backgr.htm (accessed on 13-3-2014)

Fig. 5: Fujita, T. T., 1981. Tornadoes and Downbursts in the Context of Generalized Planetary Scales. *J. Atmos. Sci.*, **38**, 1511-1534.

Fig. 6; Fig. 8; Fig. 9; Fig.10: Weisman M.L., R. Przybylinski, P. Parrish, W. Schreiber-Abshire, T. Spangler, J. Lamos, S. Jesuroga, J. Syverson and G. Byrd, 1999. The COMET Program. Mesoscale Convective Systems: Squall Lines and Bow Echoes. V3.1. *University Corporation for Atmospheric Research*.

Fig. 12: Google Earth 2013.

Fig. 14 left; Fig 15 left; EUMETSAT 2010a <http://www.woksat.info/etcsg14m/indexsg14m.html> (accessed on 2-12-2013)

Fig. 16 left; EUMETSAT 2010b <http://www.woksat.info/etcsg14/indexsg14.html> (accessed on 2-12-2013)

Appendix A, Maximum temperature contour map Europe

Fig. A1 gives a clear view of the warm temperatures of Europe. Also a clear boundary can be seen over France, which indicates the cold front described in section 1.2 Synoptic situation.

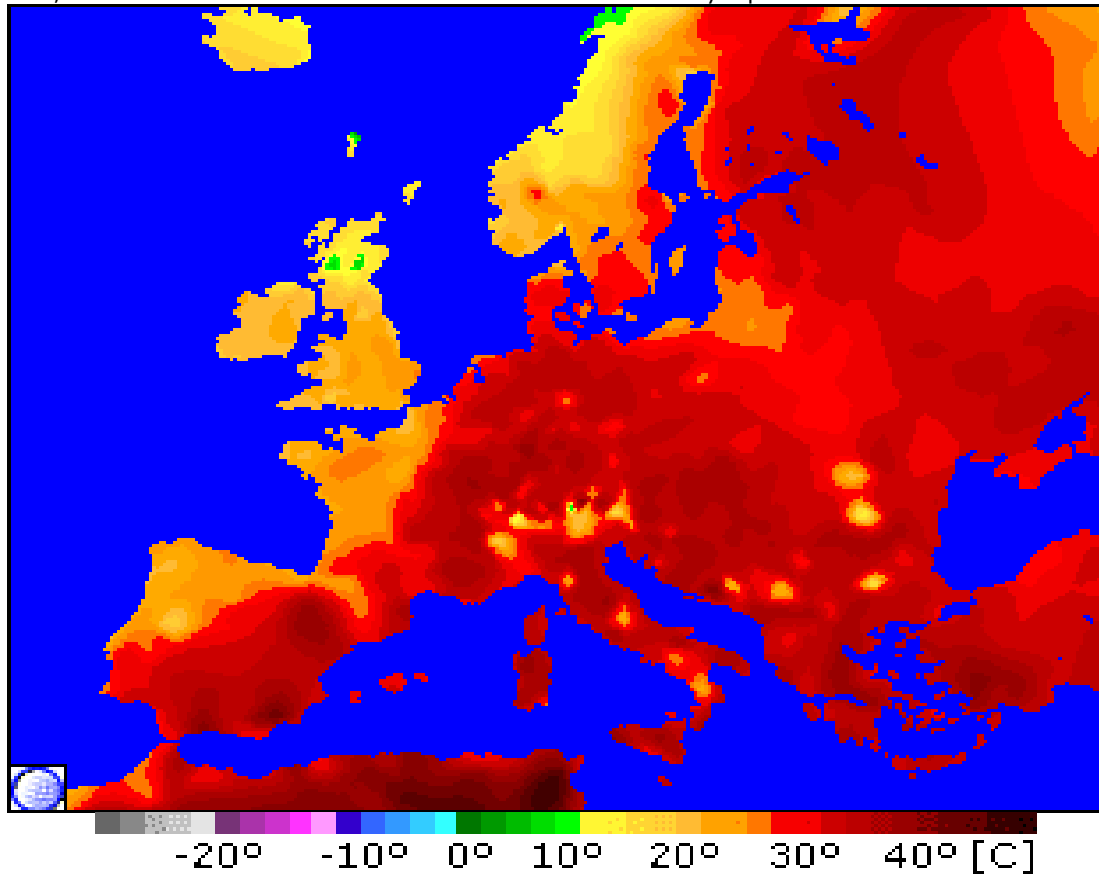


Fig. A1: Maximum temperature contour map Europe of Wednesday 14 July 2010 (WeatherOnline 2013).

WeatherOnline, 2013. Max temperature [$^{\circ}\text{C}$], Jul 14 2010.

<http://www.weatheronline.co.uk/weather/maps/current?LANG=en&CONT=euro&LAND=euro®ION=003&SORT=1&UD=0&INT=06&TYP=tmax&ART=bild&RUBRIK=akt&DATE=1279130400&CEL=C&SI=mph>
(accessed on 9-9-2013)

Appendix B, WRF default settings

	number	Name
mp_physics		*moisture scheme
ra_lw_physics	1	rrtm
ra_sw_physics	1	Dudhia
sf_sfclay_physics	2	*surface scheme
sf_surface_physics	2	Unified Noah Land-Surface Model
sf_urban_physics	0	no urbanisation
bl_pbl_physics	2	*boundary layer scheme
cu_physics	0	no cumulus

The schemes indicated with an * are variable throughout this research. The exact schemes used for each run can be seen in table 1.

Appendix C, Model performance checks

Tables for pressure and temperature performance checks, the green indicated cells are the best performing ones.

Pressure

		ME	MAE	RMSE	med-E	med-AE
MYJ + WSM6	Deelen	-6.37	6.37	6.45	-6.36	6.36
	Volkel	-2.11	2.21	2.38	-2.28	2.28
MYJ + WSM3	Deelen	-6.08	6.08	6.19	-6.19	6.19
	Volkel	-1.76	2.19	2.31	-2.07	2.16
YSU + WSM6	Deelen	-6.43	6.43	6.50	-6.51	6.51
	Volkel	-2.20	2.31	2.46	-2.37	2.37
YSU + WSM3	Deelen	-6.26	6.26	6.34	-6.36	6.36
	Volkel	-1.93	2.28	2.43	-2.32	2.35
BouLac + WSM6	Deelen	-6.44	6.44	6.49	-6.31	6.31
	Volkel	-2.12	2.30	2.44	-2.36	2.38
BouLac + WSM3	Deelen	-6.23	6.23	6.31	-6.21	6.21
	Volkel	-1.95	2.23	2.38	-2.20	2.22

Temperature

		ME	MAE	RMSE	med-E	med-AE
MYJ + WSM6	Deelen	-0.98	1.51	2.23	-0.86	1.20
	Hupsel	-1.86	2.15	2.88	-1.67	1.69
	Volkel	-1.21	1.57	2.65	-0.74	0.91
	Arcen	-1.72	2.08	3.04	-1.72	1.75
MYJ + WSM3	Deelen	-1.40	1.65	2.57	-1.12	1.17
	Hupsel	-2.11	2.27	3.07	-1.89	1.89
	Volkel	-1.45	1.60	2.63	-0.76	0.84
	Arcen	-2.02	2.10	2.92	-1.92	1.92
YSU + WSM6	Deelen	-0.79	1.47	2.32	-0.63	0.89
	Hupsel	-1.48	1.91	2.64	-1.46	1.58
	Volkel	-0.73	1.41	2.37	-0.38	0.62
	Arcen	-1.00	1.55	2.74	-0.72	1.06
YSU + WSM3	Deelen	-1.06	1.34	2.18	-0.67	0.77
	Hupsel	-1.58	1.74	2.53	-1.38	1.38
	Volkel	-1.03	1.29	2.29	-0.58	0.79
	Arcen	-1.77	1.80	2.85	-1.31	1.31
BouLac + WSM6	Deelen	-0.74	1.52	2.14	-0.54	1.14
	Hupsel	-1.52	1.99	2.58	-1.32	1.52
	Volkel	-0.98	1.62	2.44	-0.62	1.13
	Arcen	-1.31	1.80	2.52	-1.22	1.30
BouLac + WSM3	Deelen	-0.87	1.30	2.02	-0.52	1.08
	Hupsel	-1.87	2.03	2.93	-1.45	1.45
	Volkel	-1.25	1.49	2.50	-0.69	0.79
	Arcen	-1.55	1.75	2.74	-0.92	1.11

Appendix D, Overview cross-section locations



Fig. D1: Picture of the cross-section locations. Le Mans, Châlons-en-Champagne and Vethuizen (Google Earth 2013).

Appendix E, Early stage: cross-section wind and surface temperature

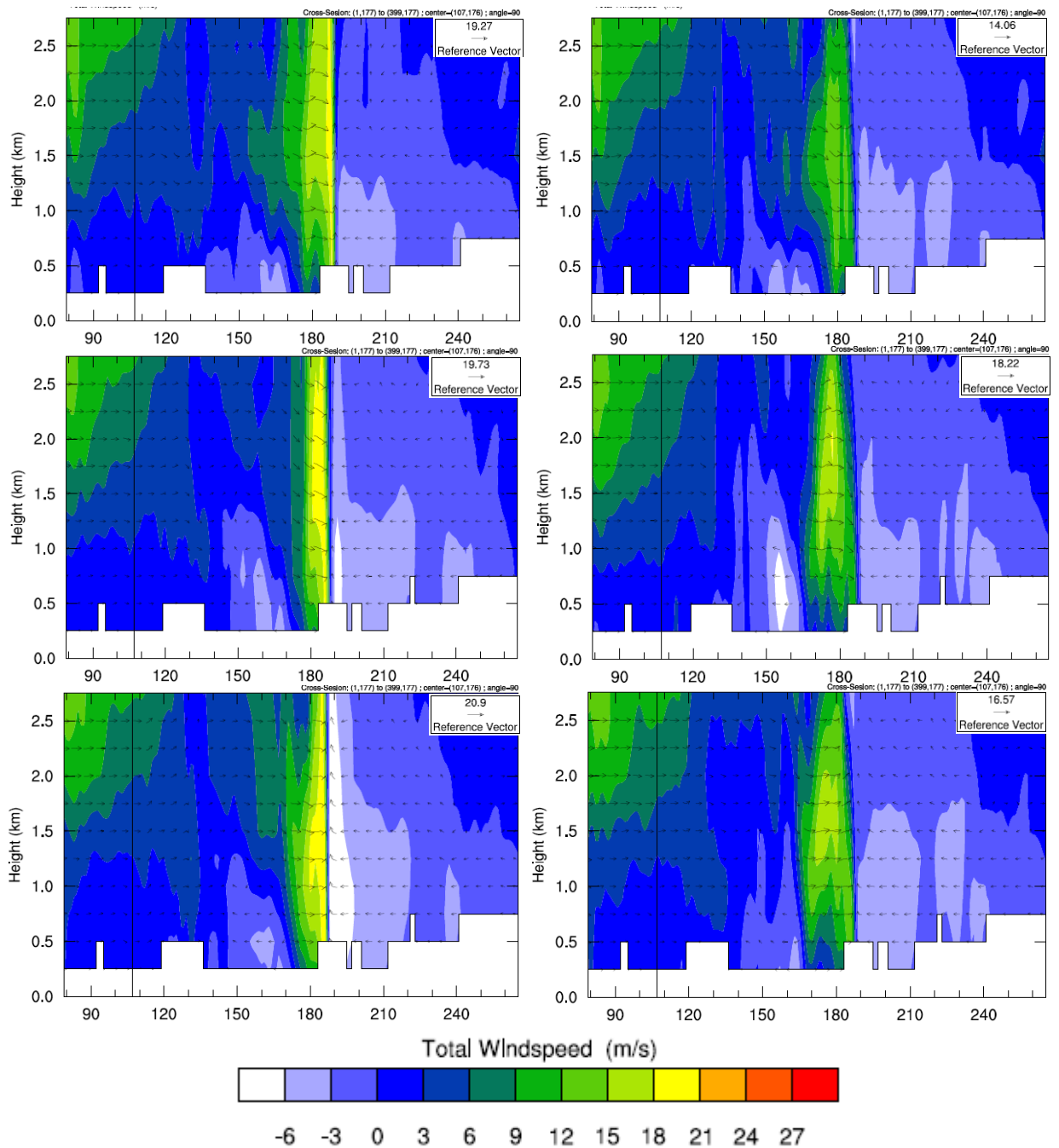


Fig. E1: Cross-section (x-axes are grid points) of the wind (shaded, m/s) and its interaction with vertical velocity (curved arrows, m/s) with the pivot point of Le Mans, France under an angle of 90 degrees (E-W orientation) at 9:00 UTC, 14 July 2010. With upper left: WSM6 + MYJ, upper right: WSM3 + MYJ, middle left: WSM6 + YSU, middle right: WSM3 + YSU, bottom left: WSM6 + BouLac and bottom right: WSM3 + BouLac. The distance between grid points is approximately 2.5km.

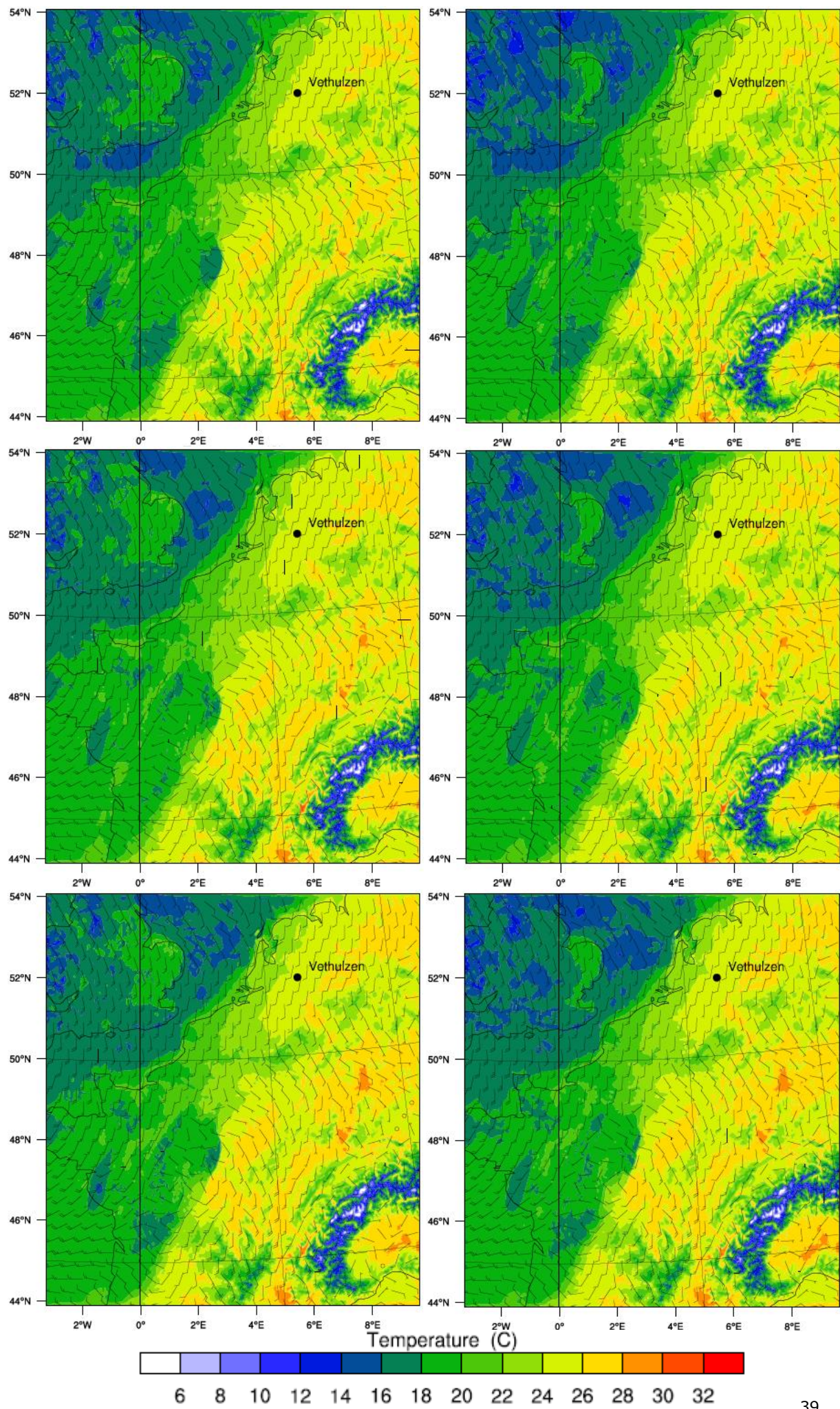


Fig. E2: Surface temperature and wind barbs (kts) of 14 July 9:00 UTC for the entire domain. With upper left: WSM6 + MYJ, upper right: WSM3 + MYJ, middle left: WSM6 + YSU, middle right: WSM3 + YSU, bottom left: WSM6 + BouLac and bottom right: WSM3 + BouLac.

Appendix F, Semi-mid stage: cross-section wind and surface temperature

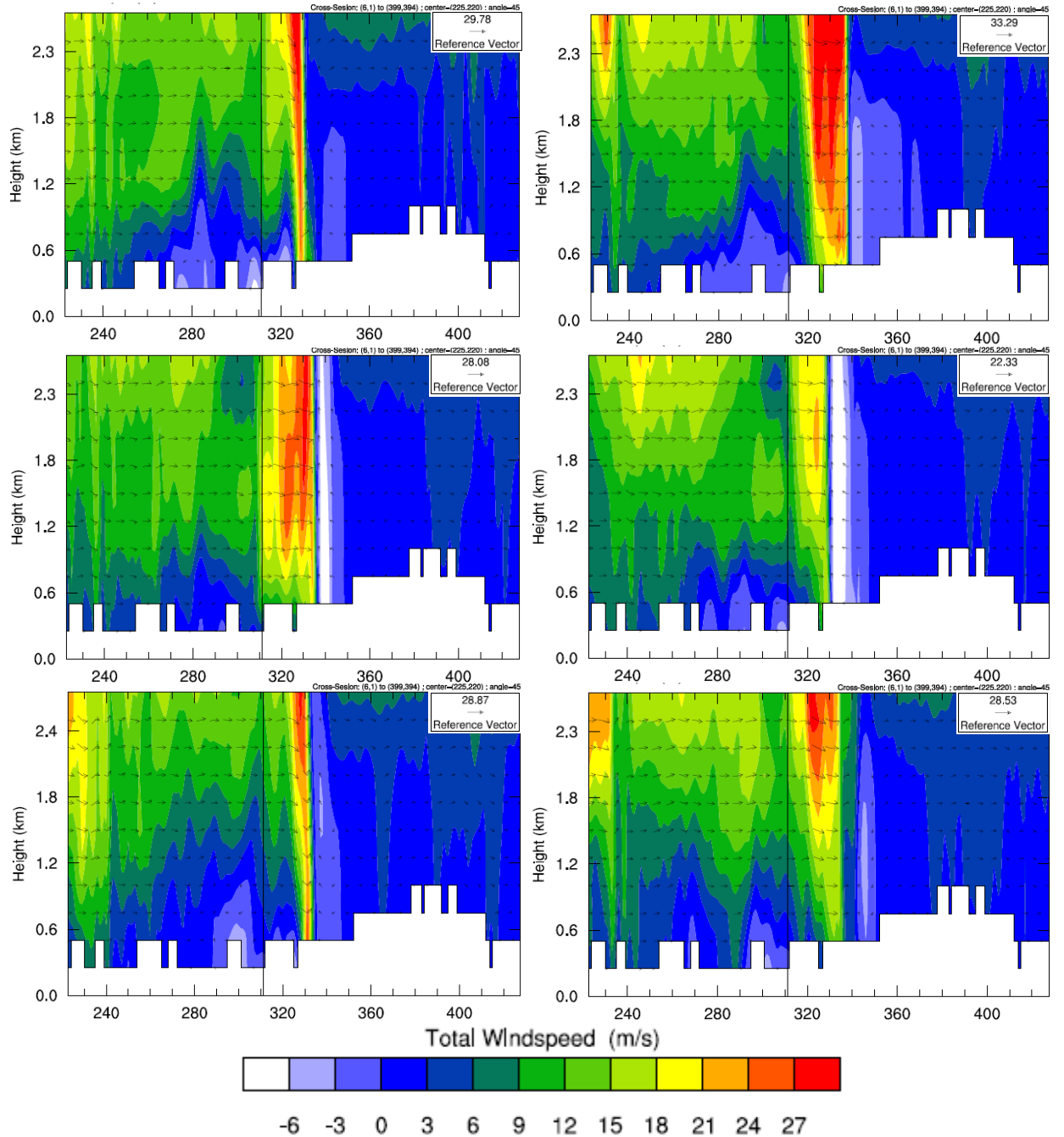


Fig. F1: Cross-section (x-axes are grid points) of the wind (shaded, m/s) and its interaction with vertical velocity (curved arrows, m/s) with the pivot point of Châlons-en-Champagne, France under an angle of 45 degrees (SE-NW orientation) at 12:00 UTC, 14 July 2010. With upper left: WSM6 + MYJ, upper right: WSM3 + MYJ, middle left: WSM + YSU, middle right: WSM3 + YSU, bottom left: WSM6 + BouLac and bottom right: WSM3 + BouLac. The distance between grid points is approximately 2.5km.

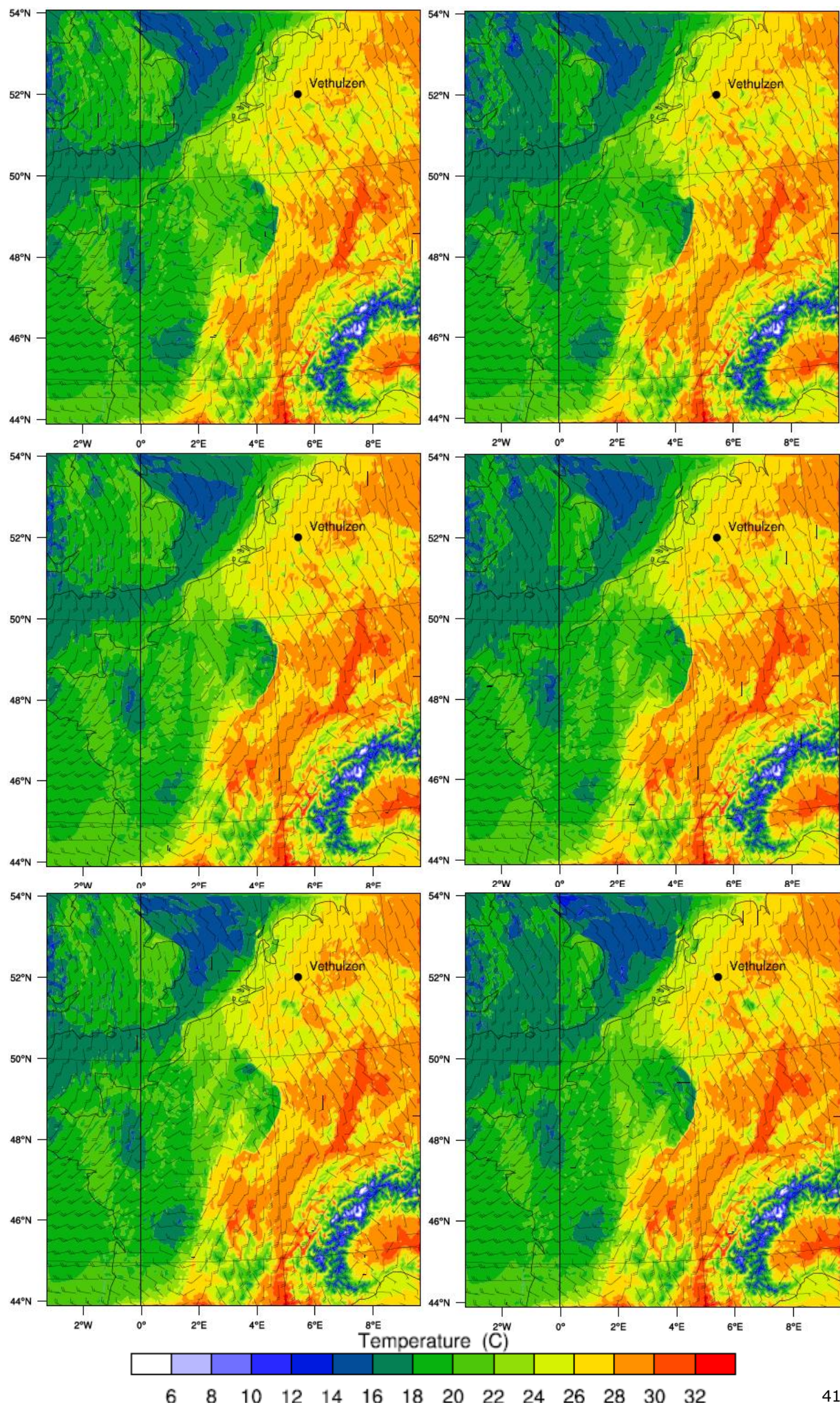


Fig. F2: Surface temperature and wind barbs (kts) of 14 July 12:00 UTC for the entire domain. With upper left: WSM6 + MYJ, upper right: WSM3 + MYJ, middle left: WSM6 + YSU, middle right: WSM3 + YSU, bottom left: WSM6 + BouLac and bottom right: WSM3 + BouLac.

Appendix G, Middle stage: cross-section wind and surface temperature

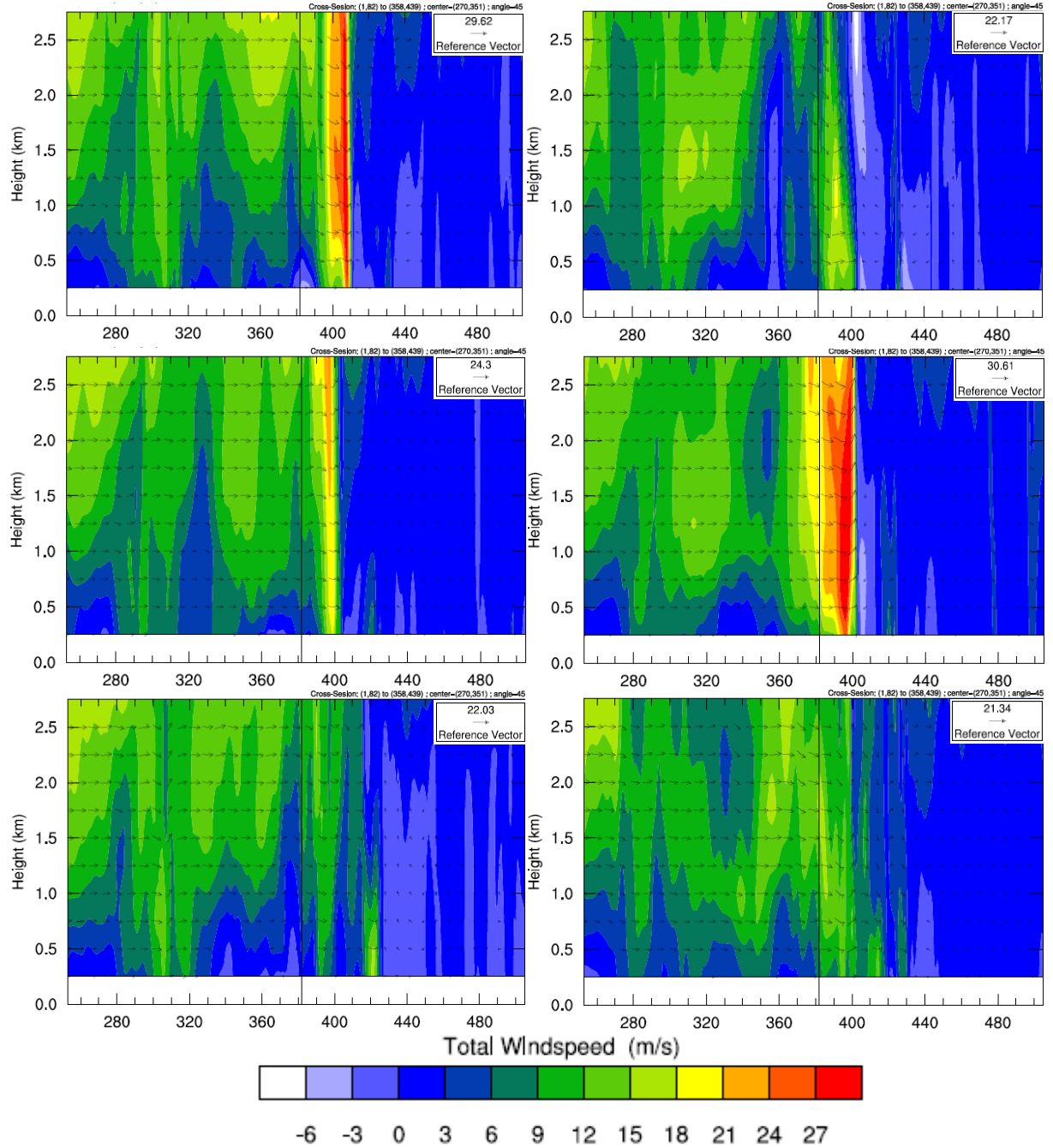


Fig. G1: Cross-section (x-axes are grid points) of the wind (shaded, m/s) and its interaction with vertical velocity (curved arrows, m/s) with the pivot point of Vethuizen, Netherlands under an angle of 45 degrees (SE-NW orientation) at 16:00 UTC, 14 July 2010. With upper left: WSM6 + MYJ, upper right: WSM3 + MYJ, middle left: WSM6 + YSU, middle right: WSM3 + YSU, bottom left: WSM6 + BouLac and bottom right: WSM3 + BouLac. The distance between grid points is approximately 2.5km.

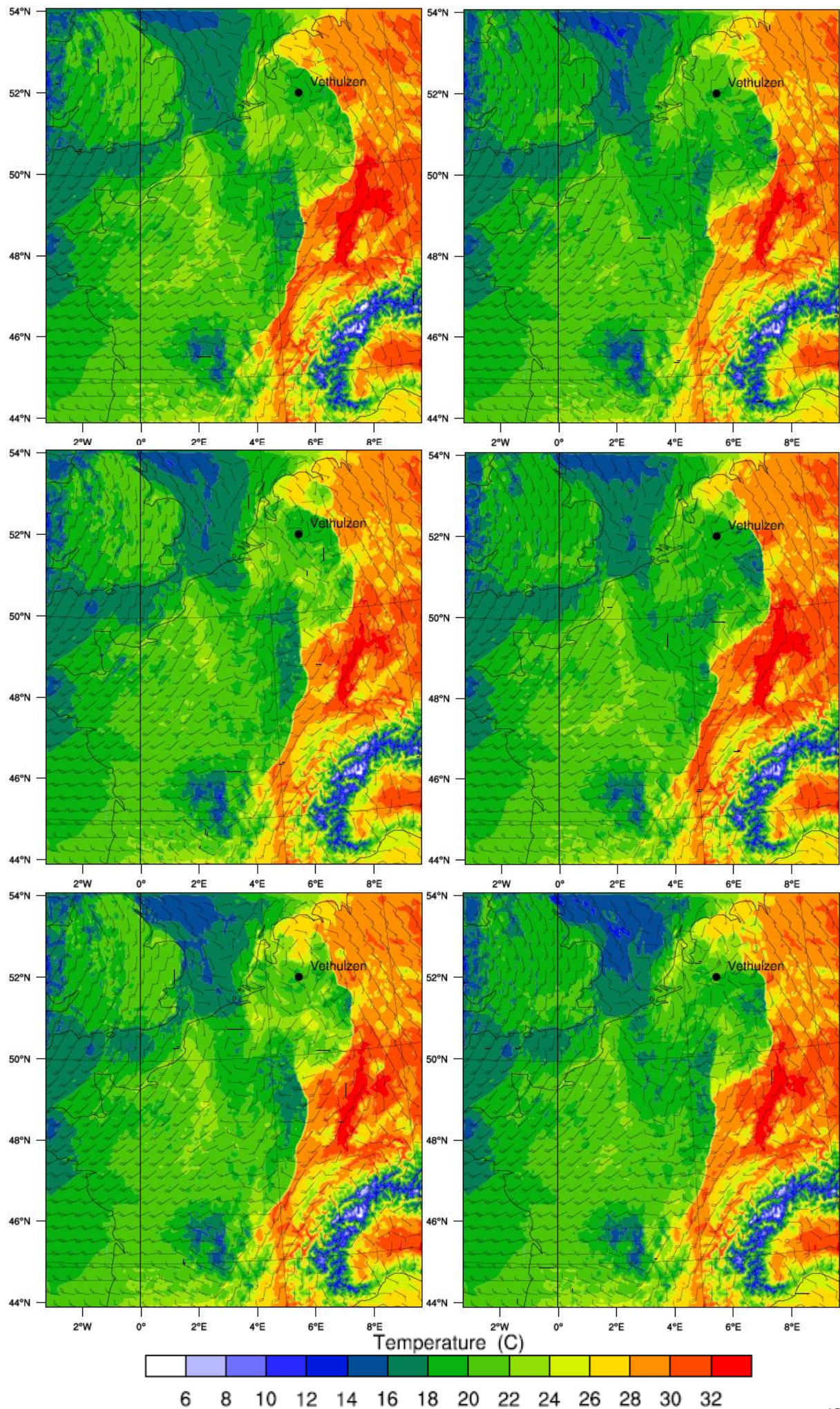


Fig. G2: Surface temperature and wind barbs (kts) of 14 July 16:00 UTC for the entire domain. With upper left: WSM6 + MYJ, upper right: WSM3 + MYJ, middle left: WSM6 + YSU, middle right: WSM3 + YSU, bottom left: WSM6 + BouLac and bottom right: WSM3 + BouLac.